institut für
theoretische physik

Bachelor's Thesis

Jet Production at the LHC

Submitted by

Jost Niehues

August 22, 2024

First Examiner: Dr. Tomáš Ježo

Second Examiner: PD. Dr. Karol Kovařík

University of Münster
Institute for Theoretical Physics

Contents

1 Indroduction

When particles subject to the strong interaction collide at high energies in particle accelerators, individual quarks and gluons are typically not seen in the final state. As they carry a color charge, they cannot exist in isolation due to confinement. Instead, they form clustered gluons and quark-antiquark pairs, which eventually convert into narrow collimated streams of hadrons known as *jets*. These jets arise close to the momentum direction of the final state particles, with highly constrained momenta transverse to the respective direction.
By studying the energy and angular distributions of the experimentally visible jets, conclusions about the involved forces and particle configurations during the collision can be drawn. Moreover, this analysis serves as a crucial component in evaluating and developing Quantum Chromodynamics (QCD), the fundamental theory describing the strong interaction.
For instance, by the late 1970s, the detection of three-jet events in bremsstrahlung phenomena, notably $e^+e^- \to q\bar{q}g \to 3\,jets$, at the PETRA electron-positron collider provided definitive evidence for the existence of the gluon. [1]

This thesis focuses on proton-proton collisions at the Large Hadron Collider (LHC). After introducing the fundamental concepts of Quantum Chromodynamics and high-energy physics, the cross section for the pp-scattering process is computed.
In a first step, the invariant amplitudes are determined analytically for processes involving either only quarks/antiquarks or only gluons. The calculation is carried out at leading order (LO), making the particles in the final state correspond to the jets observed in the experiment. In order to transition to the differential cross section for the calculated amplitudes, the basic kinematics of the collision are worked through, leading to the introduction of rapidities and transverse momenta. The resulting differential cross section is integrated using a Monte Carlo method and compared with an ATLAS detector measurement at the LHC at a center-of-mass energy of 7 TeV.

The parton model is fundamental to the entire work. In this context, the parton distribution functions $f_i(x, Q)$ (PDFs) are presented, which depend on the momentum fraction x that a parton carries inside a proton at an energy scale Q. Finally, the analysis focuses on identifying the x-regions, where the binned cross section has its largest proportion, and similarly investigates this sensitivity with respect to the given Q-scale, while evaluating the correlation between x and Q^2.

Natural units are used throughout the thesis, so that Planck constant and the speed of light are set to $\hbar = c = 1$. SI units are used for comparison with the experimental data.

2 Theoretical Background

Quantum Chromodynamics is the fundamental theory of the strong interaction, which describes the binding of quarks inside the hadrons. The exchange particles of the strong interaction are the gluons, responsible for changing the colors of the quarks. This color change is described by a non-Abelian SU(3) gauge theory, resulting in eight gluons corresponding to the eight SU(3) color transformations. The strong interaction is, when considering hadronic scales, approximately $\sim 10^2$ times stronger than the electromagnetic interaction and operates over a short range of about $\sim 1\,\mathrm{fm}$ [2].
The strength of the strong coupling constant weakens as the momentum transfer increases, what justifies a perturbative QCD approach for high energies.

2.1 Structure of the Proton

The proton is not an elementary particle; it can be decomposed into smaller electrically charged components called quarks. The nucleons' quantum numbers are defined by three quarks known as *valence quarks*. Protons consist of two up quarks (u) and one down quark (d)

$$p = |uud\rangle, \tag{2.1}$$

making it charged with $q = +1e$.
In addition, nucleons also contain *sea quarks*, which are virtual pairs of quark and antiquark, produced and annihilated in the field of strong interaction. These sea quarks include not only up and down quarks but also involve strange (s) quarks, and to a lesser extent, heavier quarks like charm (c), bottom (b) or top (t) quarks and their corresponding antiparticles. Their quantum numbers sum to zero, thus not changing the protons overall quantum numbers. Due to the electric charge of these sea quarks, it's possible to detect them in deep inelastic scattering. *Gluons* are essential for understanding the proton's internal structure, as they mediate the strong interaction between the quarks and contribute nearly half of the proton's momentum.
A key challenge when investigating these strong interactions is that experiments at the LHC are executed with hadron beams instead of the actual quarks and gluons. Consequently, a theoretical model is required to describe which particles inside the protons are colliding.
When analyzing a proton in a rapidly moving system, where the transverse momentum and the rest masses of its components are considered negligible, the structure of the proton is primarily described through the longitudinal momentum of these quasi-free constituents, which are called *partons*[3].
The partons carry the momentum fractions

$$p^{\mu}_{\mathrm{parton}} = x \cdot p^{\mu}_{L}, \tag{2.2}$$

when $p^{\mu}_{L} = |p|\,(1, 0, 0, 1)$ describes the momentum of a proton moving along the z-axis.
The probability that a momentum fraction x of the hadron is carried by a parton

i is named the *parton distribution function* $f_i(x)$. By definition, summing over all fractions results in the total momentum [4, p. 191]:

$$\sum_i \int x f_i(x)\,\mathrm{d}x = 1. \tag{2.3}$$

Since the proton consists of two up quark and one down quarks (2.1), it must hold

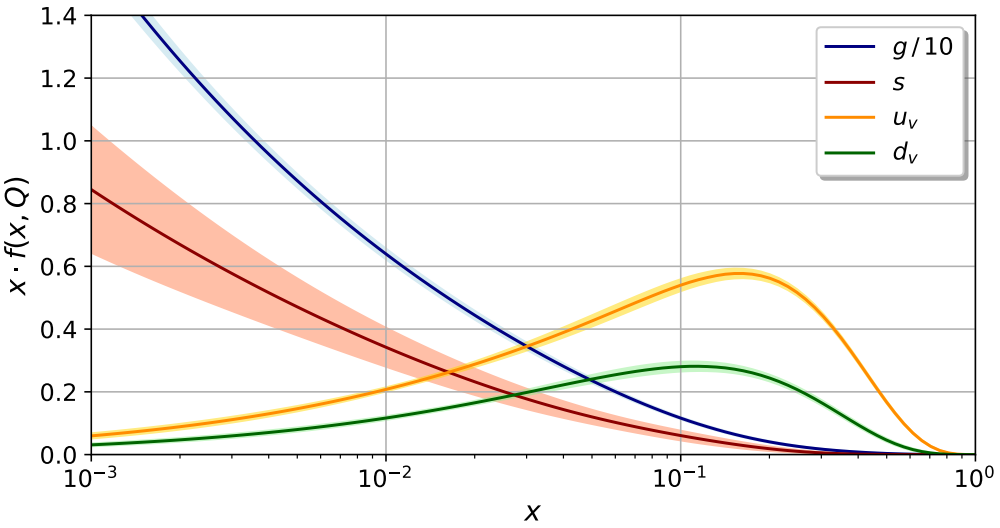

(a) $Q = 10\,\mathrm{GeV}$

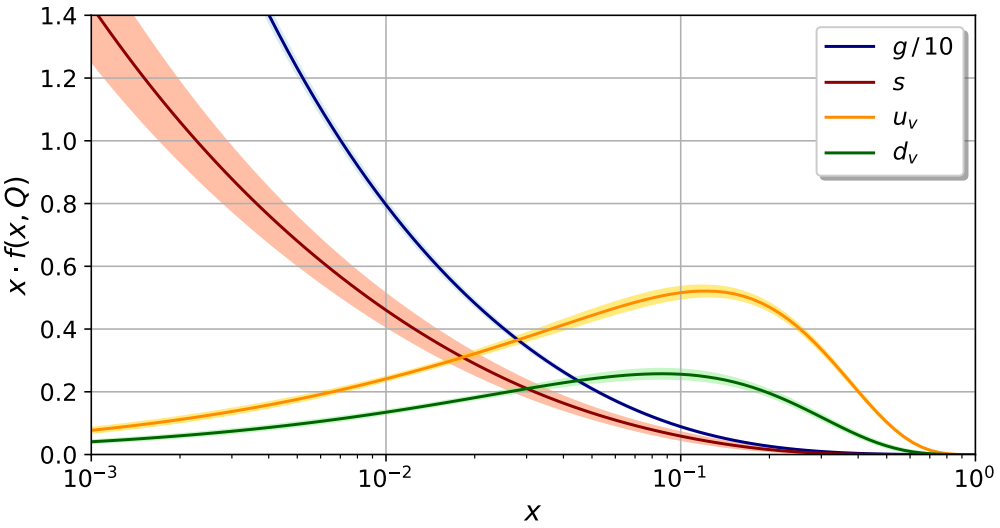

(b) $Q = 100\,\mathrm{GeV}$

Figure 1: Parton distribution function $f(x, Q)$ at different transmitted energies Q. The set of nuclear parton distribution functions used is CT18NNLO [5].

that

$$\int_0^1 (f_u - f_{\bar{u}})\,\mathrm{d}x = 2, \quad \int_0^1 (f_d - f_{\bar{d}})\,\mathrm{d}x = 1, \tag{2.4}$$

while for all other quarks within the proton these integrals should disappear.
The PDFs will be dependent on the choice of scale in the later calculation. To avoid

infrared divergences, which arise when the energy scale approaches zero, the *factorization scale* μ_f is introduced.
Figure 1 shows the PDFs for different partons depending on the transmitted energy $\mu_f = Q$ from the PDF set CT18NNLO [5]. The symbols u_v and u_d represent the valence quarks within the proton, which are determined by subtracting the antiparticle's distribution function from that of the corresponding particle.
The gluon distribution is scaled by a factor of 0.1 in the figures. It is particularly dominant for small x. Around $x \approx 10^{-1}$, the valence quarks carry the majority of the nucleons momentum. The sea quarks are primarily produced through gluon splitting, resulting in a rise of their distribution for small x while they are significantly diminished at larger x due to their larger masses.

2.2 Gauge Theory

All elementary particle interactions can be described with gauge theories, which will be motivated in the following section (based on [6] and [7]). In classical mechanics, the Lagrangian states the difference between kinetic and potential energy of a particle

$$L = T - V, \tag{2.5}$$

which is a function of the coordinates q_i and the corresponding time derivates $\dot{q}_i$.
In field theories, which treat time and space symmetrically, the transition from a discrete system to a continuous system is achieved by introducing a Lagrangian density

$$L(q_i, \dot{q}_i) \to \mathscr{L}\Big(\phi, \frac{\partial \phi}{\partial x_\mu}\Big), \tag{2.6}$$

that is a function of the fields ϕ and their space and time derivates $\frac{\partial \phi}{\partial x_\mu}$. The motion of a particle follows from the Euler-Lagrange equation, derived by varying the action

$$S = \int \mathrm{d}^4 x \mathscr{L}. \tag{2.7}$$

Free particles are described as complex fields ψ by the Lagrangian

$$\mathscr{L}_0 = \bar{\psi}(x)(i\gamma^\mu \partial_\mu - m)\psi(x) \tag{2.8}$$

from Dirac theory, which is invariant under *global* phase transformation

$$\psi \to e^{i\theta}\psi. \tag{2.9}$$

However, this symmetry cannot be just extended to invariance under *local* phase transformation where $\theta = \theta(x)$. In general, these processes are described as a multiplication of ψ by a unitary matrix

$$\psi \to U\psi, \quad U^\dagger U = 1. \tag{2.10}$$

The associated group, which includes all such matrices for the case $U = e^{i\theta}$, is the U(1) with corresponding *U(1) gauge invariance*. The demand for local phase invariance will lead to the introduction of massless vector fields and interactions between

these vector fields and particles with charge.
Requesting a local U(1) gauge invariance yields the Lagrangian of Quantum Electrodynamics (QED). The extension of this strategy results in Quantum Chromodynamics. The six different quark flavors in the Standard Model carry one of three different colors which are red, blue, green. The quark fields therefore will be described with 3-component vectors

$$\psi_{\alpha,c,f}(x), \quad \bar{\psi}_{\alpha,c,f}(x). \tag{2.11}$$

In addition to the spinor index α, the quark fields have two further indices to indicate their color ($c = 1, ..., n_c$) and flavor ($f = 1, ..., n_f$).
The QCD Lagrangian will also contain gluon fields $A^\mu_a(x)$ exchanging the strong interaction. The adjoint indices a refer to the number of generators (from 1 to 8) of the underlying system. Since a local non-Abelian SU(N)-symmetry yields to an interaction where the exchange particles also carry charges, a local
SU(3)-gauge invariance

$$\psi(x) \to U(x)\psi(x) \quad \text{with} \quad U(x) = e^{i\alpha(x)_a T_a} \tag{2.12}$$

on the free Lagrangian is requested. This is achieved by introducing a covariant derivative

$$\partial_\mu \to D_\mu = \partial_\mu - ig_s A^a_\mu T^a, \quad T^a = \frac{\lambda^a}{2}, \tag{2.13}$$

where $g_s = \sqrt{4\pi\alpha_s}$ denotes the strong coupling constant and λ^a the Gell-Mann matrices, which span the Lie Algebra of SU(3).
The commutators of the generator matrices form the structure constants of the group SU(3)

$$[T^a, T^b] = if^{abc}T^c. \tag{2.14}$$

If the normalization

$$\mathrm{Tr}(T^a T^b) = T_R \delta_{ab}, \quad T_R = \frac{1}{2} \tag{2.15}$$

is selected, the structure constants are totally antisymmetric. The color matrices obey the following relations (taken from [8]):

$$T^A T^A = C_F \mathbb{1}, \; C_F = \frac{N^2 - 1}{2N} \tag{2.16}$$

$$f^{abc} f^{abd} = C_A \delta_{cd} \quad \text{and} \quad f^{abc} f^{cde} f^{efa} = -\frac{1}{2} N f^{bdf}, \; C_A = N \tag{2.17}$$

$$T^a_{ij} T^a_{kl} = \frac{1}{2}(\delta_{il}\delta_{jk} - \frac{1}{N}\delta_{ij}\delta_{kl}). \tag{2.18}$$

For SU(3), these values are $C_F = \frac{4}{3}$ and $C_A = 3$.
With defining the gluon field strength tensor

$$F^a_{\mu\nu} = \partial_\mu A^a_\nu - \partial_\nu A^a_\mu + g_s f_{abc} A^b_\mu A^c_\nu, \tag{2.19}$$

the kinematics of the gluons are described. Finally, by adding the Yang-Mills term, the Lagrangian of QCD is expressed as

$$\mathscr{L}_{\mathrm{QCD}} = \bar{\psi_{fc}}(i\gamma^\mu D_\mu - m_f)\psi_{fc} - \frac{1}{4} F^a_{\mu\nu} F^{a\mu\nu}, \tag{2.20}$$

where summation over c and f is implied.
The Dirac matrices γ^μ are important for the following calculations, with useful relations provided in appendix A.1.

2.3 Feynman Rules

Each Lagrangian results in a set of Feynman Rules, which are outlined here without being explicitly derived.
As seen in the previous section, the Lagrangian is formed by a free Lagrangian for the participating field and associated interaction terms. The free Lagrangian corresponds to the propagators, whereas the interaction terms correlate with the vertex factors. Expanding the Lagrangian 2.20 by plugging in eq. 2.19 illustrates the gluon self-interaction, as higher order terms of the gluon fields appear. This explains the presence of the three-gluon ($\sim A^3$) and four-gluon ($\sim A^4$) vertices discussed in this section.
The external lines describe the participating particles, where the direction of the arrow indicates whether particles (left to right) or antiparticles (right to left) are involved. Each particle is provided with a factor depending on its spin s

$$s = \frac{1}{2} \Rightarrow \begin{cases} \text{incoming particle} : u \\ \text{incoming antiparticle} : \bar{v} \\ \text{outgoing particle} : \bar{u} \\ \text{outgoing antiparticle} : v \end{cases}$$

Here, u and v are spinors with four components, which can be derived from solving the Dirac Equation. They satisfy the completeness relation

$$\begin{aligned} \sum_s u_{s,\alpha}(p)\, \bar{u}_{s,\beta}(p) &= (\not{p} + m)_{\alpha\beta} \\ \sum_s v_{s,\alpha}(p)\, \bar{v}_{s,\beta}(p) &= (\not{p} - m)_{\alpha\beta}, \end{aligned} \tag{2.21}$$

where the Feynman slash notation was introduced. The $4x4$ matrix $\not{p}$ is defined as

$$\not{p} \equiv p_\mu \gamma^\mu$$

for a four-vector p_μ.

For spin-1 particles follows

$$s = 1 \Rightarrow \begin{cases} \text{incoming particle} : \epsilon \\ \text{outgoing particle} : \epsilon^*, \end{cases}$$

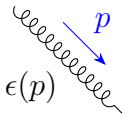

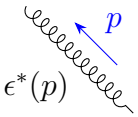

where ϵ represents the particle's spin and consists of four components.
While massive spin-1 particles exhibit three polarization states, massless gauge bosons as the gluon have only two states of polarization. The polarization must be perpendicular to the direction of movement of the gluons, so that $p^\mu \epsilon_\mu = 0$.
Therefore, they satisfy the completeness relation

$$\sum_\lambda \epsilon_\lambda^{\mu*}(p)\epsilon_\lambda^\nu(p) = -g^{\mu\nu} + \frac{p^\mu \tilde{p}^\nu + p^\mu \tilde{p}^\nu}{p \cdot \tilde{p}}, \tag{2.22}$$

summed over the possible polarization states.
For the upcoming calculations, only gluon propagators have to be considered. The gluons carry not only a momentum, but also a color charge:

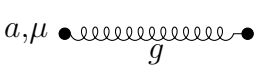

$$= -i\delta_{ab}\frac{g^{\mu\nu}}{q^2}. \tag{2.23}$$

Furthermore, the QCD rules important for this thesis can be introduced:

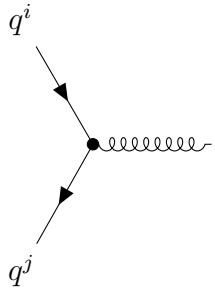

$$= ig_s\gamma_\mu T^a_{ij} \tag{2.24}$$

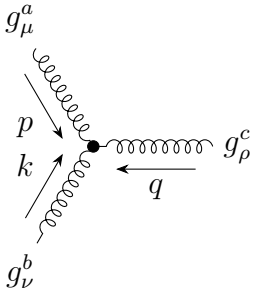

$$= g_s f^{abc}[g_{\mu\nu}(p-k)_\rho + g_{\nu\rho}(k-q)_\mu + g_{\rho\mu}(q-p)_\nu] \tag{2.25}$$

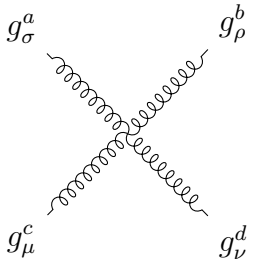

$$\begin{aligned} &= -ig_s^2[f^{cae}f^{bde}(g_{\mu\rho}g_{\sigma\nu} - g_{\mu\nu}g_{\sigma\rho}) \\ &\quad + f^{cde}f^{abe}(g_{\mu\sigma}g_{\rho\nu} - g_{\mu\rho}g_{\sigma\nu}) \\ &\quad + f^{cbe}f^{dae}(g_{\mu\nu}g_{\sigma\rho} - g_{\mu\sigma}g_{\rho\nu})]. \end{aligned} \tag{2.26}$$

2.4 Strong Coupling Constant

A coupling constant α characterizes the strength of interaction between two particles.
The calculation of amplitudes corresponding to higher order Feynman diagrams containing loops can lead to ultraviolet divergences [1], which necessitate the process of renormalization. That results in a so-called *running* coupling constant $\alpha_s(\mu_r^2)$, which is large at low energy and smaller at high energy. It is a function of a (unphysical) renormalization scale μ_r. For μ_r close to the momentum transfer Q scale, $\alpha_s(\mu_r^2 \simeq Q^2)$ represents the effective strength of the strong interaction in that process [9].

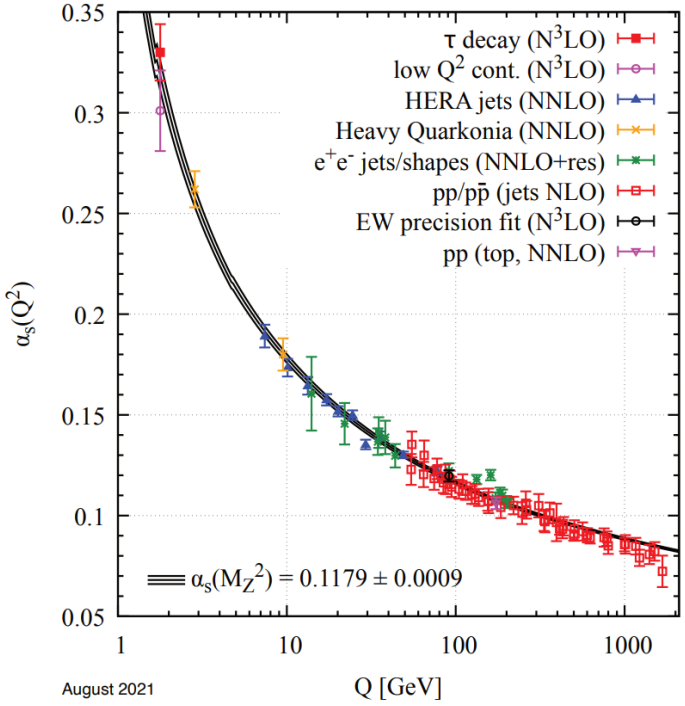

Figure 2: The theoretical prediction of the running coupling constant as a function of the renormalization scale Q compared to the experimental data. Source: [10, p. 164]

It obeys the following renormalization group equation [10, p. 149]

$$\mu_r^2 \frac{\mathrm{d}\alpha_s}{\mathrm{d}\mu_r^2} = \beta_{\mathrm{QCD}}(\alpha_s) = -(b_0\alpha_s^2 + b_1\alpha_s^3 + \mathcal{O}(\alpha_s^4)), \tag{2.27}$$

with the perturbative expansion of the QCD β-function.
Taking only the lowest order into account leads to

$$\alpha_s(\mu_r^2) = \frac{1}{b_0 \ln(\frac{\mu_r^2}{\Lambda^2})} = \frac{12\pi}{(33 - 2n_f) \cdot \ln(\frac{\mu_r^2}{\Lambda^2})}, \tag{2.28}$$

[1] closed loops in the propagator lead to a divergence of the integral as the momentum running inside the loop approaches infinity.

where n_f is the number of light quarks ($m_q \ll \mu_r$) and $\Lambda \approx 200\,\text{MeV}$ is the QCD scale parameter, where the coupling constant diverges. The value of Λ indicates the energy scale where perturbation theory remains applicable ($\mu_r \gg \Lambda$) [3, p. 108].
Due to the minus sign in eq. 2.27, it follows that $\beta < 0$ for $n_f < 17$, which leads to *asymptotic freedom*. This describes that the coupling in the limes $Q^2 \to \infty$ becomes arbitrarily weak, which is a strong contrast to QED. At lower energies and greater distances, the coupling constant grows so rapidly that it becomes impossible to separate individual quarks from hadrons, illustrating the concept of *confinement*. In this region, the perturbative approach to solutions of the strong interaction at low energies must be discarded, whereas the asymptotic freedom gives the possibility to expand the α_s.
The PDFs discussed in section 2.1 are sensitive to the value of $\alpha_s(\mu_r^2)$. Usually the scale is set to the mass of the Z-boson. The contributing measurements are presented in figure 2 and yield an average of [10, p. 160]

$$\alpha_s(M_Z^2) = 0.1179 \pm 0.0009. \tag{2.29}$$

2.5 Jet Definition

In QCD, interactions involving quarks and gluons result in outgoing quarks and gluons as well. Due to confinement (see chapter 2.4) these particles do not form asymptotic states and thus remain undetectable, since the strength of their interactions grows with increasing distance. Rather, they form a beam of hadrons (e.g.

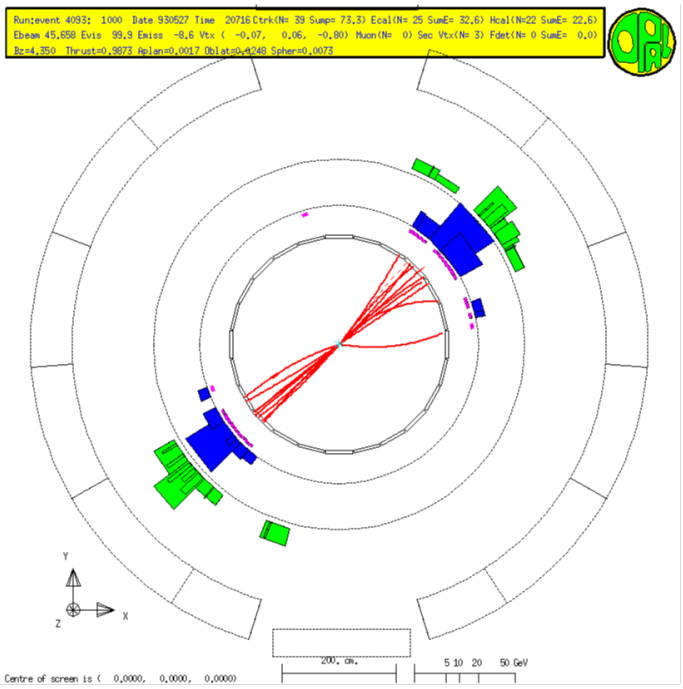

Figure 3: A Z^0-Boson decays two quarks that are visible in the detector as two back-to-back jets. Source: [11]

pions, kaons,...), what is called a *jet*. By measuring the jets, the kinematics of the elementary QCD processes can be reconstructed. According to the conservation of

energy and momentum, the momentum of the hadrons lies within a cone around the original quark or gluon momentum as can be seen in the two-jet event in figure 3. A jet describes a concentration of transverse energy, with the cone defined by a radius R, which is given by [12, p. 247]:

$$R = \sqrt{(\Delta\eta)^2 + (\Delta\phi)^2}. \tag{2.30}$$

Here $\eta = -\ln(\theta/2)$ is the pseudorapidity with the angle θ of the beam direction and ϕ states the azimuthal angle. As already discussed, in leading order calculations, the parton in the final state corresponds to the jet. This means that influences of the cone size only appear in next-to-leading order (NLO) predictions, whereby the cross section increases as the cone becomes wider.
The beam generated by a hard parton is clustered with jet algorithms. The later experimental data are based on a sequential one, the anti-k_T algorithm [13]. The anti-k_T jet algorithm identifies and reconstructs jets by using the transverse momentum of the particles to calculate distances between pairs of particles as well as to the jet. It connects pairs with minimum distances iteratively until all particles are grouped into jets. In the end, the final jet corresponds to the reconstructed hard partons from which the shower was formed.

2.6 Monte Carlo Methods

The error of numerical quadrature methods in d dimensions with n function evaluations, such as the trapezoidal rule ($\sim n^{-2/d}$) or Simpson's rule ($\sim n^{-4/d}$), depends on the dimension. In contrast, Monte Carlo integration does not exhibit this dependency, as its error scales with $1/\sqrt{n}$ regardless of the dimension. The following description is based on [14] and [15].

2.6.1 Monte Carlo Integration

Consider a d-dimensional integral of a function $f(x)$

$$I = \int \mathrm{d}x\, f(x) \tag{2.31}$$

integrated over the unit hypercube $[0,1]^d$. This integral can be approximated by defining the Monte Carlo estimate

$$f_n = \frac{1}{n}\sum_{i=1}^{n} f(x_i), \tag{2.32}$$

where $\{x_i\}_{i=1}^n$ are independent samples drawn from a uniform distribution over $[0,1]^d$. The law of large numbers ensures that f_n converges to the real value I of the integral. According to the Central Limit Theorem, the sample mean of a random variable is approximately normal $N(\mu, \sigma^2/n)$ distributed, which allows estimating the error as follows:

$$\sigma^2 = \int (f(x) - I)^2\, \mathrm{d}x \approx \frac{1}{n}\sum_{i=1}^{n}(f(x_i) - f_n)^2 = \frac{1}{n}\sum_{i=1}^{n} f(x_i)^2 - f_n^2. \tag{2.33}$$

This analysis demonstrates that the error scales with $1/\sqrt{n}$, regardless of the dimension. To minimize the statistical fluctuations inherent in random sampling, the next sections introduce variance reducing techniques.

2.6.2 Importance Sampling

It is possible to reduce the variance by selecting a distribution $p(x)$[2] for the random variables such that the density of the sampling points closely matches the form of the integrand. This method is called *importance sampling*, whereas the integral is rewritten as

$$I = \int \frac{f(x)}{p(x)} p(x)\,\mathrm{d}x \tag{2.34}$$

and approximated by

$$f_n = \frac{1}{n}\sum_{i=1}^{n} \frac{f(x_i)}{p(x_i)}, \tag{2.35}$$

with variance given by eq. 2.33 for $f(x_i) \to f(x_i)/p(x_i)$.
This clarifies the essence of importance sampling: If p is chosen in a shape similar to that of f, the ratio $\frac{f}{p}$ becomes approximately constant and the variance is reduced.

2.6.3 Stratified Sampling

With *stratified sampling* the domain of integration is divided into k subspaces M_j $(j = 1, ..., k)$, whereby different sample sizes n_j for the different parts are used. The resulting Monte Carlo approximation is:

$$f_n = \sum_{j=1}^{k} \frac{\mathrm{vol}(M_j)}{n_j} \sum_{i=1}^{n_j} f(x_{ij}). \tag{2.36}$$

The total error

$$u_{\mathrm{sts}} = \sqrt{\sum_{j=1}^{k} \frac{\mathrm{vol}(M_j)^2}{n_j} \sigma^2_{M_j}(f)}, \tag{2.37}$$

arises from the individual errors in estimating the contribution of each region M_j to the overall integral. Here, $\sigma^2_{M_j}(f)$ represents the variance of the function f within region M_j, calculated as:

$$\sigma^2_{M_j}(f) = \frac{1}{\mathrm{vol}(M_j)} \int_{M_j} f(x)^2\,\mathrm{d}x - \left(\frac{1}{\mathrm{vol}(M_j)} \int_{M_j} f(x)\,\mathrm{d}x\right)^2. \tag{2.38}$$

The optimal performance is reached, when

$$n_j \sim \mathrm{vol}(M_j)\sigma_{M_j}(f) \tag{2.39}$$

applies to the number of evaluations.

[2] $p(x)$ fulfills the properties of a probability density function, ensuring that $p(x)$ is normalized to 1 and $p(x) \leq 0$.

2.6.4 Vegas Algorithm

The adaptive Monte Carlo algorithm VEGAS [16] utilizes the two variance reduction methods described above. The algorithm starts by dividing the hypercube into smaller pieces of an identical size and samples in each of them. The integration grid is then optimized for the next iteration using the previous results for approximating the best probability density function

$$p_{\text{Vegas}}(\vec{x}) = \frac{|f(\vec{x})|}{\int_0^1 \mathrm{d}^d\vec{x}|f(\vec{x})|}. \tag{2.40}$$

The grid is decomposed by factorizing p in d dimensions into p_i in each dimension

$$p(\vec{x}) = \prod_{i=1}^{d} p_i(x_i). \tag{2.41}$$

Once the optimal grid has been found after some iterations with few sampling points, the integral is now calculated with the fixed grid and higher precision.
In each iteration j, an estimate f_{jn} and variance σ_{jn}^2 according to eq. 2.35 is evaluated. The results of each iteration are summarized into a cumulative estimate

$$f_n = \left(\sum_{j=1}^{m} \frac{n_j}{\sigma_{jn}^2}\right)^{-1} \left(\sum_{j=1}^{m} \frac{n_j f_{jn}}{\sigma_{jn}^2}\right), \tag{2.42}$$

where each estimator is weighted by the number of sampling points n_j and corresponding variance.
The reliability of the whole evaluation is classified by the χ^2- function

$$\chi^2 \simeq \sum_j \frac{(f_{jn} - f_n)^2}{\sigma_{jn}^2}. \tag{2.43}$$

The returned value should not exceed the number of iterations for a trustworthy procedure.
A more recent version of the VEGAS algorithm [17] uses adaptive stratified sampling, where the integrand samples are redistributed across the hypercubes after each iteration according to eq. 2.39.

3 Two-Jet Amplitudes

If an incoming parton from one proton collides with a parton from another proton, the result is the production of two partons possessing a high transverse momentum, which are observed as jets. This section will focus on calculating the transition amplitudes at the partonic level for specific jet production processes by utilizing the rules outlined in chapter 2.3.
This thesis considers only tree-level diagrams. It should be noted that real and virtual gluon corrections to the discussed processes will introduce higher-order terms to the perturbative series.[3]
For the first channels including quarks, a strict order for setting up the amplitude is necessary to have matching matrix multiplications.
Starting with a fermion line, it will be traced backward through the diagram, recording all line factors, propagators, and vertex factors sequentially from left to right. What will be achieved is a combination consisting of an adjoint spinor, a 4×4 matrix and a spinor, yielding in a scalar upon completion of the calculation ([6, Chapter 7.5]).

3.1 Quark-Antiquark Scattering

The first process that is considered is the scattering of a quark with an antiquark of the same flavor ($q_i\bar{q}_i \to q_i\bar{q}_i$). Since two different processes (see fig. 4a, 4b) are obtained, there will be an interference term when calculating the total matrix element

$$|M|^2 = |M_s + M_t|^2 = |M_s|^2 + |M_t|^2 + 2\mathrm{Re}(M_s M_t^\dagger). \tag{3.1}$$

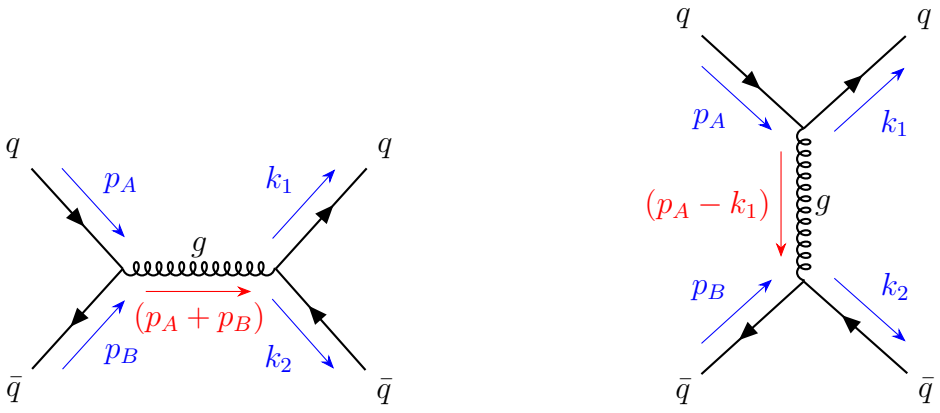

(a) s-channel (b) t-channel

Figure 4: Feynman diagrams for the scattering process $q\overline{q} \to q\overline{q}$ in leading order with definition of the parton momenta.

The s-channel seen in fig. 4a is the first to be analyzed. By convention, incoming particles will always have a momentum p, while outgoing particles will have a mo-

[3] In tree diagrams the conservation of momentum at each vertex is mandatory, while this cannot be hold for diagrams containing loops.

mentum k. By applying the Feynman rules for the gluon propagator 2.23 and the quark-gluon vertex 2.24, the amplitude is written as

$$\begin{aligned} M_s &= \Big[\bar{v}(p_B)\cdot ig_s\gamma^\mu T^a_{kl}\cdot u(p_A)\Big]\left(-i\frac{\delta^{ab}}{q^2}g^{\mu\nu}\right)\Big[\bar{u}(k_1)\cdot ig_s\gamma^\nu T^b_{nm}\cdot v(k_2)\Big] \\ &= i\frac{g_s^2}{s}\cdot \underbrace{T^a_{kl}T^a_{nm}}_{M_{\text{col}}}\cdot \underbrace{\Big[\bar{v}(p_B)\gamma^\mu u(p_A)\bar{u}(k_1)\gamma_\mu v(k_2)\Big]}_{M_p}, \end{aligned} \tag{3.2}$$

where $q^2=(p_A+p_B)^2=s$ is a Mandelstam variable (see appendix A.2).
Using the relations of the gamma matrices, the corresponding adjoint results in

$$\begin{aligned} M_s^\dagger &= \frac{g_s^2}{s}\cdot \underbrace{T^b_{mn}T^b_{lk}}_{M_{\text{col}}^\dagger}\cdot\Big[u(p_A)^\dagger(-i\gamma^{\mu\dagger})\gamma^0 v(p_B)\Big]\cdot ig^{\mu\nu}\cdot\Big[v(k_2)^\dagger(-i\gamma^{\nu\dagger})\gamma^0 u(k_1)\Big] \quad |\bar{v}=v^\dagger\gamma^0 \\ &= -i\frac{g_s^2}{s}\cdot M_{\text{col}}^\dagger\cdot\Big[\bar{u}(p_A)\gamma^0\gamma^{\mu\dagger}\gamma^0 v(p_B)\Big]\cdot g^{\mu\nu}\cdot\Big[\bar{v}(k_2)\gamma^0\gamma^{\nu\dagger}\gamma^0 u(k_1)\Big] \\ &= -i\frac{g^2}{s}\cdot M_{\text{col}}^\dagger\cdot \underbrace{\Big[\bar{u}(p_A)\gamma^\nu v(p_B)\bar{v}(k_2)\gamma_\nu u(k_1)\Big]}_{M_p^\dagger} \quad |\gamma^{\mu\dagger}=\gamma^0\gamma^\mu\gamma^0. \end{aligned} \tag{3.3}$$

Here, M_{col} represents the contribution from the color charge and M_p denotes the contribution from the momentum.
For an unpolarized cross section, the amplitude should be independent of spin and color of the incoming quarks, because no information about the spins is detected. Therefore, the matrix elements are averaged over all possible spin directions s_A, s_B and colors N from the incoming quarks and summed over the spins of the particles in the final state:

$$\overline{|M|}^2 = \frac{1}{(2s_A+1)(2s_B+1)}\frac{1}{N^2}\sum_s MM^\dagger = \frac{1}{36}\sum_s |M|^2. \tag{3.4}$$

Using the completeness relation 2.21 along with the Feynman slash notation, the momentum component can be expressed in the form

$$\begin{aligned} |M_{s,p}|^2 &= \Big[\bar{v}_a(p_B)\gamma^\mu_{ab}u_b(p_A)\bar{u}_c(k_1)\gamma_{\mu,cd}v_d(k_2)\Big] \\ &\qquad\cdot\Big[\bar{u}_e(p_A)\gamma^\nu_{ef}v_f(p_B)\bar{v}_g(k_2)\gamma_{\nu,gh}u_h(k_1)\Big] \\ &= \Big[(\not{p}_B-m)_{fa}\gamma^\mu_{ab}(\not{p}_A+m)_{be}\gamma^\nu_{ef}\Big]\cdot\Big[(\not{k}_1+m)_{hc}\gamma_{\mu,cd}(\not{k}_2-m)_{dg}\gamma_{\nu,gh}\Big], \end{aligned} \tag{3.5}$$

with indices added to improve the clarity of the subsequent calculation.
For the sake of clarity, this has again been divided into two parts, where the first one will be examined exemplarily by factorizing, finding traces and using the identities

from A.8:

$$\begin{aligned}
|M_{s,p_1}|^2 &= (p_B^\alpha \gamma_\alpha - m)_{fa}\gamma^\mu_{ab} \cdot (p_A^\beta \gamma_\beta + m)_{be}\gamma^\nu_{ef} \\
&= \Big[(p_B^\alpha \gamma_\alpha)_{fa}\gamma^\mu_{ab} - m\delta_{fa}\gamma^\mu_{ab}\Big] \cdot \Big[(p_A^\beta \gamma_\beta)_{be}\gamma^\nu_{ef} + m\delta_{be}\gamma^\nu_{ef}\Big] \\
&= p_B^\alpha p_A^\beta \operatorname{Tr}(\gamma_\alpha\gamma^\mu\gamma_\beta\gamma^\nu) + \cancel{p_B^\alpha m \operatorname{Tr}(\gamma_\alpha\gamma^\mu\gamma^\nu)} - \cancel{p_A^\beta m \operatorname{Tr}(\gamma_\mu\gamma_\beta\gamma^\nu)} - m^2 \operatorname{Tr}(\gamma^\mu\gamma^\nu) \\
&= 4p_B^\alpha p_A^\beta (g^\mu_\alpha g^\nu_\beta - g_{\alpha\beta}g^{\mu\nu} + g^\nu_\alpha g^\mu_\beta) - 4m^2 g^{\mu\nu} \\
&= 4p_B^\mu p_A^\nu - 4(p_B \cdot p_A)g^{\mu\nu} + p_B^\nu p_A^\mu - 4m^2 g^{\mu\nu} \\
&= 4\Big[p_A^\mu p_B^\nu + p_A^\nu p_B^\mu - (p_A \cdot p_B + m^2)g^{\mu\nu}\Big].
\end{aligned} \tag{3.6}$$

Analogously follows for $|M_{s,p_2}|^2$:

$$|M_{s,p_2}|^2 = 4\Big[k_{1\mu}k_{2\nu} + k_{1\nu}k_{2\mu} - (k_1 \cdot k_2 + m^2)g_{\mu\nu}\Big]. \tag{3.7}$$

From this point on, the quark masses are disregarded since subsequent collision energies of order TeV are considered, making the proton's rest mass negligible.
Taking the results from eq. 3.6 and 3.7, the whole kinematic contribution is calculated as

$$\begin{aligned}
|M_{s,p}|^2 &= 4\Big[p_A^\mu p_B^\nu + p_A^\nu p_B^\mu - (p_A \cdot p_B)g^{\mu\nu}\Big] \cdot 4\Big[k_{1\mu}k_{2\nu} + k_{1\nu}k_{2\mu} - (k_1 \cdot k_2)g_{\mu\nu}\Big] \\
&= 16\Big[2(p_A \cdot k_1)(p_B \cdot k_2) + 2(p_A \cdot k_2)(p_B \cdot k_1) \\
&\qquad + 4(p_A \cdot p_B)(k_1 \cdot k_2) - 4(p_A \cdot p_B)(k_1 \cdot k_2)\Big] \\
&= 8(u^2 + t^2).
\end{aligned} \tag{3.8}$$

For the color part, the relation 2.15 for the generators of a SU(N) algebra is needed, as given in the theoretical introduction:

$$\begin{aligned}
|M_{\mathrm{s,col}}|^2 &= T^a_{kl}T^b_{lk}\,T^a_{nm}T^b_{mn} \\
&= \operatorname{Tr}(T^aT^b)^2 = (\frac{1}{2}\delta_{ab})^2 = \frac{1}{4}\delta_{aa} \\
&= \frac{1}{4}(N^2 - 1),
\end{aligned} \tag{3.9}$$

where $\delta_{aa} = (N^2 - 1)$ with Einstein notation was used. All in all, the invariant matrix element averaged over color and spin can be written in the form

$$\overline{|M_s|}^2 = \frac{g_s^4}{4N^2} \cdot \frac{N^2 - 1}{4} \cdot 8\frac{u^2 + t^2}{s^2}, \tag{3.10}$$

which leads to

$$\frac{1}{g_s^4}\overline{|M_s|}^2 = \frac{4}{9}\frac{u^2 + t^2}{s^2} \tag{3.11}$$

for $N = 3$ colors.

The second diagram that has to be determined is the t-channel shown in figure

4b. With the same approach as above, the invariant amplitude and the associated conjugate can be stated as

$$M_t = \Big[\bar{v}(p_B)\cdot ig_s\gamma^\mu T^a_{km}\cdot v(k_2)\Big]\left(-i\frac{\delta^{ab}}{t}g^{\mu\nu}\right)\Big[\bar{u}(k_1)\cdot ig_s\gamma^\nu T^b_{nl}\cdot u(p_A)\Big] \tag{3.12}$$

$$M_t^\dagger = -i\frac{g_s^2}{t}T^b_{ln}T^b_{mk}\Big[\bar{v}(k_2)\gamma^\nu v(p_B)\bar{u}(p_A)\gamma_\nu u(k_1)\Big]. \tag{3.13}$$

Furthermore the color factor in $|M_t|^2$ remains unchanged, whereas the momentum contribution is calculated using the completeness relation and the trace identities. The outcome shares a similar structure with equation 3.6 and equation 3.7 when neglecting the mass terms:

$$\begin{aligned}|M_{t,p}|^2 &= \Big[\bar{v}(p_B)\gamma^\mu v(k_2)\bar{u}(k_1)\gamma_\mu u(p_A)\Big]\cdot\Big[\bar{v}(k_2)\gamma^\nu v(p_B)\bar{u}(p_A)\gamma_\nu u(k_1)\Big]\\ &= 4\Big[k_2^\mu p_B^\nu k_2^\nu + p_B^\mu - (k_2\cdot p_B)g^{\mu\nu}\Big]\cdot 4\Big[k_{1\mu}p_{A\nu} + k_{1\nu}p_{A\mu} - (k_1\cdot p_A)g_{\mu\nu}\Big]\\ &= 32\Big[(p_B\cdot k_1)(k_2\cdot p_A) + (p_B\cdot p_A)(k_2\cdot k_1)\Big]\\ &= 8(u^2+s^2).\end{aligned} \tag{3.14}$$

This is also the expected outcome when the s-channel is transformed into the t-channel by exchanging the momenta $p_B \leftrightarrow -k_1$. Therefore, the squared amplitude results with averaging and the color term in

$$\frac{1}{g_s^4}\overline{|M_t|}^2 = \frac{4}{9}\frac{u^2+s^2}{t^2}. \tag{3.15}$$

The final step in obtaining the total invariant amplitude is to calculate the interference between the two channels.
In the s-channel, there is an overall minus sign for the amplitude, which was neglected for the squared matrix element. Nevertheless, this minus sign must be taken into account for the interference term, resulting in a negative sign in front of the real part in formula 3.1. This negative sign arises from the antisymmetrization of fermion wave functions (refer to [18, p. 120] for additional details).
The interference follows as

$$\begin{aligned}M_sM_t^\dagger &= \frac{g_s^4}{st}\cdot T^a_{kl}T^a_{nm}\Big[\bar{v}(p_\mathrm{B})\gamma^\mu u(p_\mathrm{A})\bar{u}(k_1)\gamma_\mu v(k_2)\Big]\\ &\quad\cdot T^b_{mk}T^b_{ln}\Big[\bar{v}(k_2)\gamma^\nu v(p_B)\bar{u}(p_A)\gamma_\nu u(k_1)\Big]\\ &= \frac{g_s^4}{st}\cdot\underbrace{T^a_{kl}T^a_{nm}T^b_{mk}T^b_{ln}}_{(M_sM_t^\dagger)_\mathrm{col}}\cdot\underbrace{[\not{p}_\mathrm{B}\gamma^\mu\not{p}_\mathrm{A}\gamma_\nu]\cdot[\not{k}_1\gamma_\mu\not{k}_2\gamma^\nu]}_{(M_sM_t^\dagger)_p}.\end{aligned} \tag{3.16}$$

With equation 2.18 the determination of the color part yields:

$$\begin{aligned}(M_sM_t^\dagger)_\mathrm{col} &= T^a_{kl}T^a_{nm}T^b_{mk}T^b_{ln}\\ &= \frac{1}{4}\Big(\delta_{km}\delta_{ln} - \frac{1}{N}\delta_{kl}\delta_{nm}\Big)\Big(\delta_{mn}\delta_{kl} - \frac{1}{N}\delta_{mk}\delta_{ln}\Big)\\ &= \frac{1}{4}\Big(\delta_{nn} - \frac{2}{N}\delta_{ll}\delta_{mm} + \frac{1}{N^2}\delta_{mm}\Big)\quad|\delta_{mm}=3\\ &= -\frac{2}{3}\quad|N=3.\end{aligned} \tag{3.17}$$

After adding indices in eq. 3.16, a trace can be identified for the momentum part. This trace can be further analyzed using the trace theorem provided in app. A.8:

$$\begin{aligned}
(M_s M_t^\dagger)_p &= \not{p}_{B,fa}\,\gamma^\mu_{ab}\,\not{p}_{A,bg}\,\gamma_{\nu,gh}\,\not{k}_{1,hc}\gamma_{\mu,cd}\,\not{k}_{2,de}\,\gamma^\nu_{ef} \\
&= p_B^\alpha p_A^\beta k_1^\sigma k_2^\rho \ \mathrm{Tr}(\gamma_\alpha\gamma^\mu\gamma_\beta\gamma_\nu\gamma_\sigma\gamma_\mu\gamma_\rho\gamma^\nu) \\
&= -2p_B^\alpha p_A^\beta k_1^\sigma k_2^\rho \ \mathrm{Tr}(\gamma_\alpha\gamma_\sigma\gamma_\nu\gamma_\beta\gamma_\rho\gamma^\nu) \quad |\gamma^\mu\gamma_\beta\gamma_\nu\gamma_\sigma\gamma_\mu = -2\gamma_\sigma\gamma_\nu\gamma_\beta \\
&= -8p_B^\alpha p_A^\beta k_1^\sigma k_2^\rho \, g_{\beta\rho}\,\mathrm{Tr}(\gamma_\alpha\gamma_\sigma) \quad |\gamma_\nu\gamma_\beta\gamma_\rho\gamma^\nu = 4g_{\beta\rho} \\
&= -32p_B^\alpha p_A^\beta k_1^\sigma k_2^\rho \, g_{\beta\rho}g_{\alpha\sigma} \\
&= -32(p_B\cdot k_1)(p_A\cdot k_2) \\
&= -8u^2.
\end{aligned} \tag{3.18}$$

Merging the two partial results according to eq. 3.1 leads to an overall amplitude

$$\frac{1}{g_s^4}\overline{|M_{q_i\bar{q}_i\to q_i\bar{q}_i}|}^2 = \frac{4}{9}\Big(\frac{u^2+t^2}{s^2}+\frac{u^2+s^2}{t^2}\Big) - \frac{8}{27}\frac{u^2}{st} \tag{3.19}$$

for the quark-antiquark scattering process.

After determining the matrix element of the $q_i\overline{q_i} \to q_i\overline{q_i}$ process, all other $2\to 2$ collision processes containing quarks and antiquarks (flavor indices i, j) can be derived from it.
The processes in question are:

- $q_i\overline{q}_j \to q_i\overline{q}_j$
- $q_i\overline{q}_i \to q_j\overline{q}_j$
- $q_iq_i \to q_iq_i$
- $q_iq_j \to q_iq_j$
- $\overline{q}_i\overline{q}_i \to \overline{q}_i\overline{q}_i$
- $\overline{q}_i\overline{q}_j \to \overline{q}_i\overline{q}_j$.

Starting with $q_i\overline{q}_j \to q_i\overline{q}_j$, only the t-channel 4b is possible,
while for $q_i\overline{q}_i \to q_j\overline{q}_j$ only the s-channel 4a survives. Since the quarks now differ from each other ($i \neq j$), continuous fermion lines are no longer possible in the respective vanishing Feynman diagrams. As a consequence, the results from 3.15 and 3.11 are transferred.
For the quark-quark scattering processes, new Feynman diagrams must be obtained, in accordance with figure 5. Since the color component remains the same as discussed in chapter 3.1, it is sufficient to only analyze the momentum factors. For the amplitude of the t-channel follows

$$|M_{t,p}|^2 = [\bar{u}(k_2)\gamma^\mu u(p_B)\bar{u}(k_1)\gamma_\mu u(p_A)]\cdot[\bar{u}(p_B)\gamma^\nu u(k_2)\bar{u}(p_A)\gamma_\nu u(k_1)]\,. \tag{3.20}$$

Correspondingly, the lower fermion line in the diagram has to be reversed, i.e. $\bar{u}(k_2) \to \bar{v}(p_B)$ and $u(p_B) \to v(k_2)$. Since the completeness relations for the spinors

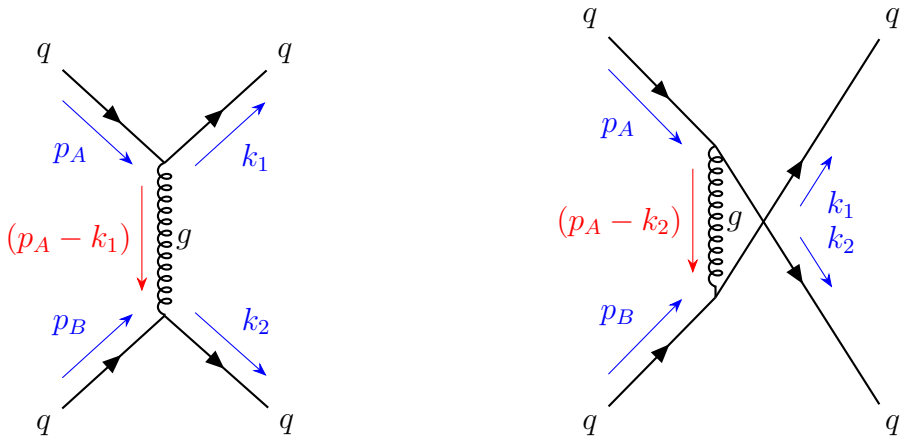

(a) t-channel (b) u-channel

Figure 5: Feynman diagrams for the $qq \to qq$ scattering process.

$u(p), v(p)$ do not differ from each other when neglecting masses and the calculation is invariant under changing k_2 and p_B, the result remains

$$\frac{1}{g_s^4}\overline{|M_{t,qq}|}^2 = \frac{4}{9}\frac{u^2+s^2}{t^2}. \tag{3.21}$$

The u-channel can be inferred from the t-channel by crossing. This requires swapping the momenta $k_1 \leftrightarrow k_2$, which results in the Mandelstam variable t being replaced by u:

$$\frac{1}{g_s^4}\overline{|M_{u,qq}|}^2 = \frac{4}{9}\frac{t^2+s^2}{u^2}. \tag{3.22}$$

For the interference term, the momenta must be switched ($k_2 \leftrightarrow -p_B$) for the transition from s-channel to u-channel. This leads again just to an interchange of the Mandelstam variables, this time s and u. All in all the invariant amplitude for quark-quark scattering results in

$$\frac{1}{g_s^4}\overline{|M_{q_iq_i\to q_iq_i}|}^2 = \frac{4}{9}\Big(\frac{t^2+s^2}{u^2} + \frac{u^2+s^2}{t^2}\Big) - \frac{8}{27}\frac{s^2}{ut}. \tag{3.23}$$

Accordingly, only the contribution of the t-channel remains for the $q_iq_j \to q_iq_j$ process. The same results as above are also obtained for the two antiquark processes ($\overline{q}_i\overline{q}_i \to \overline{q}_i\overline{q}_i$, $\overline{q}_i\overline{q}_j \to \overline{q}_i\overline{q}_j$), since only the directions of the fermion lines are reversed. Concluding, all amplitudes can be derived from the calculations of the quark-antiquark scattering with a quark of a single flavor ($q_i\overline{q}_i \to q_i\overline{q}_i$) just by exchanging the momenta. It was important for the argumentation to neglect the masses of the quarks.

3.2 Gluon-Gluon Scattering

In this section, the matrix element for gluon-gluon interaction with gluons in the final state ($gg \to gg$) will be derived. In particular, there are four different processes, see fig. 6, that have to be considered.

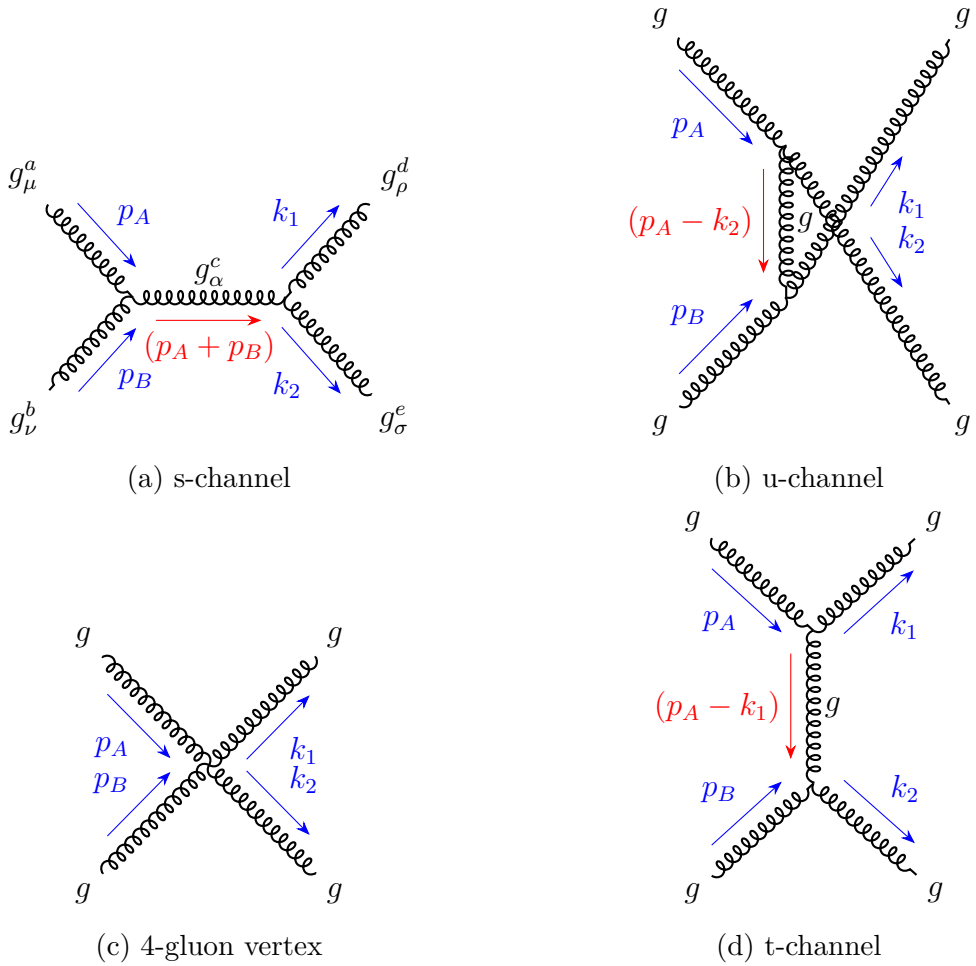

(a) s-channel

(b) u-channel

(c) 4-gluon vertex

(d) t-channel

Figure 6: The four different Feynman diagrams for the $gg \to gg$-scattering.

Beginning with diagram 6a, the s-channel amplitude is determined by applying the Feynman rules for the three-gluon vertex 2.25 as

$$\begin{aligned}
|M_{gg/s}|^2 =& \epsilon_\mu(p_A)\epsilon_\nu(p_B)\epsilon^*_\rho(k_1)\epsilon^*_\sigma(k_2) \cdot \epsilon^*_\chi(p_A)\epsilon^*_\phi(p_B)\epsilon_\gamma(k_1)\epsilon_\xi(k_2) \\
&\cdot [g_{\mu\nu}(p_A - p_B)_\alpha + g_{\nu\alpha}(p_B + q_s^2)_\mu + g_{\alpha\mu}(-q_s^2 - p_A)_\nu] \\
&\cdot [g_{\beta\sigma}(q_s^2 + k_2)_\rho + g_{\sigma\rho}(-k_2 + k_1)_\beta + g_{\rho\beta}(-k_1 - q_s^2)_\sigma] \\
&\cdot [g_{\chi\phi}(p_A - p_B)_\omega + g_{\phi\omega}(p_B + q_s^2)_\chi + g_{\omega\chi}(-q_s^2 - p_A)_\phi] \\
&\cdot [g_{\eta\xi}(q_s^2 + k_2)_\gamma + g_{\xi\gamma}(-k_2 + k_1)_\eta + g_{\gamma\eta}(-k_1 - q^2)_\xi] \\
&\cdot \frac{g_s^4}{s^2} g^{\alpha\beta} g^{\omega\eta} \cdot \underbrace{f^{abc} f^{abh} f^{ced} f^{hed}}_{|M_{gg,col}|^2} \\
=& |M_{gg/s,p}|^2 \cdot |M_{gg,col}|^2,
\end{aligned} \tag{3.24}$$

where $q_s^2 = (p_A + p_B)^2$ denotes the momentum transfer. If a momentum comes out of the vertex, the sign must be inverted.
For ease of reading, the calculation is divided into two parts. The contribution of the color carried by the gluons is obtained by making use of the relation of the structure constants in eq. 2.17:

$$|M_{gg,col}|^2 = f^{abc} f^{abh} f^{ced} f^{hed} = N\delta_{ch} \cdot N\delta_{ch} = N^2(N^2 - 1). \tag{3.25}$$

This factor is the same for s-, t- and u-channel, but will vary for the interference terms.
The massless gluon is transversely polarized and has two directions of polarization. In the completeness relation 2.22 the vector $\tilde{p}$ is free to choose, but cannot be perpendicular to the momentum p, so that $p \cdot \tilde{p} \neq 0$.
A reasonable choice if $p = p_A$ is to let $\tilde{p} = p_B$ and to set $\tilde{p} = p_A$ when $p = p_B$, since this ensures $p \cdot \tilde{p} = \frac{1}{2}s$, which is non-zero. This reasoning also holds for k_1 and k_2.
The calculation for the momentum part is done with the FeynCalc package [19] in Mathematica [20] and leads to

$$|M_{gg/s,p}|^2 = -g_s^4 \frac{4(s^4 + s^2(-3t^2 + 2tu - 3u^2) + (t^2 - u^2)^2)}{s^2}. \tag{3.26}$$

Taking into account that s, t and u are not independent of each other, since $s + t + u = 0$ for masseless particles, the momentum amplitude simplifies to

$$|M_{gg/s,p}|^2 = g_s^4 \frac{4(s + 2t)^2}{s^2}. \tag{3.27}$$

The computation for the t-channel follows a similar process, although the momenta need to be modified when utilizing the three-gluon vertex rule:

$$\begin{aligned} M_{gg/t} = -i\frac{g_s^2}{t} \cdot M_{gg,col} \cdot \epsilon_\mu(p_A)\epsilon_\rho^*(k_1)\epsilon_\nu(p_B)\epsilon_\sigma^*(k_2) \cdot g^{\lambda\gamma} \\ \cdot [g_{\mu\rho}(p_A + k_1)_\lambda + g_{\rho\lambda}(-k_1 + q_t)_\mu + g_{\lambda\mu}(-q_t - p_A)_\rho] \\ \cdot [g_{\nu\sigma}(p_B + k_2)_\gamma + g_{\sigma\gamma}(-k_2 - q_t)_\nu + g_{\gamma\nu}(q_t - p_B)_\sigma]. \end{aligned} \tag{3.28}$$

It ensues with FeynCalc:

$$|M_{gg/t,p}|^2 = g_s^4 \frac{4(4s^6 + 4s^5t + 17s^4t^2 + 36s^3t^3 + 24s^2t^4 + 8st^5 + 4t^6)}{s^4t^2}. \tag{3.29}$$

The amplitude of the u-channel can be determined by applying the same rules. For the u-channel the result is

$$|M_{gg/u,p}|^2 = g_s^4 \frac{4(s^6 + 2s^5t + 33s^4t^2 + 60s^3t^3 + 44s^2t^4 + 16st^5 + 4t^6)}{s^4(s + t)^2}. \tag{3.30}$$

When calculating the amplitude of the four-gluon vertex, color and momentum are inseparable

$$\begin{aligned} M_{gg/4} = -ig_s^2\epsilon_\mu(p_A)\epsilon_\rho^*(k_1)\epsilon_\nu(p_B)\epsilon_\sigma^*(k_2) \cdot \\ [f^{bec}f^{adc}(g_{\nu\mu}g_{\rho\sigma} - g_{\nu\rho}g_{\mu\sigma}) + f^{bdc}f^{eac}(g_{\nu\sigma}g_{\mu\rho} - g_{\nu\mu}g_{\rho\sigma}) \\ + f^{bac}f^{dec}(g_{\nu\rho}g_{\mu\sigma} - g_{\nu\sigma}g_{\mu\rho})]. \end{aligned} \tag{3.31}$$

Multiplication with the corresponding adjoint and insertion of the polarization sums 2.22 results in

$$|M_{gg/4}|^2 = \frac{6N^2(N^2-1)(3s^4+8s^3t+16s^2t^2+16st^3+8t^4)}{s^4}. \tag{3.32}$$

In addition to the amplitudes of the four diagrams in figure 6, there will be six interference terms. Since the calculation can be separated into a momentum and color factor, the computation for the s-, t-, and u-channel is done first:

$$M_s M_u^\dagger = g_s^4 \cdot M_{\text{col,int}} \cdot \frac{-2(s^4-5s^3t-22s^2t^2-18st^3-4t^4)}{s^3(s+t)} \tag{3.33}$$

$$M_t M_u^\dagger = g_s^4 \cdot M_{\text{col,int}} \cdot \frac{2(2s^6-9s^5t+19s^4t^2+48s^3t^3+4s^2t^4-24st^5-8t^6)}{s^4t(s+t)} \tag{3.34}$$

$$M_s M_t^\dagger = g_s^4 \cdot M_{\text{col,int}} \cdot \frac{-2(2s^4+s^3t-8s^2t^2-2st^3+4t^4)}{s^3t}. \tag{3.35}$$

Evaluating the color factors $M_{\text{col,int}}$

$$\begin{aligned}(M_s M_u^\dagger)_{gg,col} &= f^{abc}f^{ced}\cdot f^{ake}f^{kbd}\\ &= f^{abc}(-f^{cde})(-f^{eka})f^{kbd}\\ &= -\frac{1}{2}Nf^{bdk}f^{kbd} = -\frac{1}{2}N^2(N^2-1)\end{aligned} \tag{3.36}$$

$$\begin{aligned}(M_t M_u^\dagger)_{gg,col} &= f^{adc}f^{cbe}\cdot(-f^{eka})f^{kbd}\\ &= \frac{1}{2}Nf^{dbk}f^{kbd} = -\frac{1}{2}N^2(N^2-1),\end{aligned} \tag{3.37}$$

$$\begin{aligned}(M_s M_t^\dagger)_{gg,col} &= f^{abc}f^{ced}\cdot f^{dka}f^{bek}\\ &= -\frac{1}{2}Nf^{bek}f^{bek} = -\frac{1}{2}N^2(N^2-1)\end{aligned} \tag{3.38}$$

reveals that they do not differ from each other.
The calculation for the interference terms including the four-gluon vertex shows, that the interference with the s-channel vanishes:

$$M_4 M_s^\dagger = 0 \tag{3.39}$$

$$M_4 M_t^\dagger = g_s^4 \frac{-6N^2(N^2-1)t(6s^4+11s^3t+9s^2t^2+8st^3+4t^4)}{s^4t} \tag{3.40}$$

$$M_4 M_u^\dagger = g_s^4 \frac{6N^2(N^2-1)t(s^3-9s^2t-8st^2-4t^3)}{s^4}. \tag{3.41}$$

Adding up all partial results, averaging over all spins and colors in the initial state

and summing over the spins in the final state, the result is

$$\begin{aligned}\frac{1}{g_s^4}\overline{|M_{gg\to gg}|}^2 &= \frac{1}{4}\frac{1}{(N^2-1)^2}\Big(|M_{gg,col}|^2\cdot\left(|M_{gg/s,p}|^2+|M_{gg/t,p}|^2+|M_{gg/u,p}|^2\right)\\ &\quad +|M_{gg/4}|^2+2\cdot\left(M_4M_u^\dagger+M_4M_t^\dagger+M_sM_u^\dagger+M_tM_u^\dagger+M_sM_t^\dagger\right)\Big)\\ &= \frac{32\cdot N^2}{4\cdot 2\cdot(N^2-1)}\frac{(s^2+st+t^2)^3}{s^2t^2(s^2+t^2)}\\ &= \frac{9}{2}\left(3-\frac{t\cdot u}{s^2}-\frac{s\cdot u}{t^2}-\frac{s\cdot t}{u^2}\right),\end{aligned} \tag{3.42}$$

for $N=3$ colors.
Table 1 lists all channels calculated so far as well as those involving gluon-quark interactions (calculations not included in the thesis), where i,j represent different quark flavor indices.

Process	$\overline{\sum}\|M\|^2/g_s^4$
$q_i\bar{q}_i\to q_i\bar{q}_i$	$\frac{4}{9}\left(\frac{s^2+u^2}{t^2}+\frac{u^2+t^2}{s^2}\right)-\frac{8}{27}\frac{u^2}{st}$
$q_i\bar{q}_j\to q_i\bar{q}_j$	$\frac{4}{9}\frac{s^2+u^2}{t^2}$
$q_i\bar{q}_i\to q_j\bar{q}_j$	$\frac{4}{9}\frac{t^2+u^2}{s^2}$
$q_iq_i\to q_iq_i$	$\frac{4}{9}\left(\frac{t^2+s^2}{u^2}+\frac{u^2+s^2}{t^2}\right)-\frac{8}{27}\frac{s^2}{ut}$
$q_iq_j\to q_iq_j$	$\frac{4}{9}\frac{s^2+u^2}{t^2}$
$\bar{q}_i\bar{q}_i\to \bar{q}_i\bar{q}_i$	$\frac{4}{9}\left(\frac{t^2+s^2}{u^2}+\frac{u^2+s^2}{t^2}\right)-\frac{8}{27}\frac{s^2}{ut}$
$\bar{q}_i\bar{q}_j\to \bar{q}_i\bar{q}_j$	$\frac{4}{9}\frac{s^2+u^2}{t^2}$
$gg\to gg$	$\frac{9}{2}\left(3-\frac{tu}{s^2}-\frac{su}{t^2}-\frac{st}{u^2}\right)$
$gg\to q_i\bar{q}_i$	$\frac{1}{6}\frac{t^2+u^2}{tu}-\frac{3}{8}\frac{t^2+u^2}{s^2}$
$q_i\bar{q}_i\to gg$	$\frac{32}{27}\frac{t^2+u^2}{tu}-\frac{8}{3}\frac{t^2+u^2}{s^2}$
$gq_i\to gq_i$	$-\frac{4}{9}\frac{s^2+u^2}{su}+\frac{u^2+s^2}{t^2}$
$g\bar{q}_i\to g\bar{q}_i$	$-\frac{4}{9}\frac{s^2+u^2}{su}+\frac{u^2+s^2}{t^2}$

Table 1: Scattering processes and corresponding matrix elements for jet production compared with [12, p. 249].

4 Kinematics

After calculating the matrix elements, the next step is to take a look at the kinematics of a proton-proton collision for determining the cross section.
The differential cross section is defined as the number of detected particles $\mathrm{d}N$ per incoming particle density flow j_{in} and solid angle element $\mathrm{d}\Omega$:

$$\frac{\mathrm{d}\sigma}{\mathrm{d}\Omega} = \frac{\mathrm{d}N}{j_{\text{in}}\mathrm{d}\Omega}. \tag{4.1}$$

It is necessary to consider two distinct reference systems for the collision. One is the **hadron center of mass system (HCMS)** in which the protons collide. The momenta are counter-directed, so

$$\vec{P_1} + \vec{P_2} = 0, \tag{4.2}$$

where P_i denotes the momentum of the respective proton. The invariant mass is given by $\sqrt{s}$, which becomes clear when using eq. 4.2:

$$\begin{aligned} s = (P_1 + P_2)^2 &= (E_{p_1} + E_{p_2})^2 - \underbrace{(\vec{P_2} + \vec{P_2})}_{=0} = (E_{p_1} + E_{p_2})^2 \\ \hookrightarrow E_{\text{HCMS}} &= E_{p_1} + E_{p_2} = \sqrt{s}. \end{aligned} \tag{4.3}$$

The protons collide with the same energy, meaning that the energy is separated symmetrically $E_{p_1} = E_{p_2} = \frac{\sqrt{s}}{2}$. Choosing the coordinate system such that the particles enter along the z-axis causes the momentum components in $x-$ and $y-$direction to disappear. Considering the relativistic energy-momentum relation in the massless limit, the momentum component in z-direction corresponds to the energy of the proton $P_{1,z} = \frac{\sqrt{s}}{2} = -P_{2,z}$.

The momenta of the partons are defined by a fragment of the proton's momentum

$$\vec{p_1} = x_1\vec{P_1} \quad \& \quad \vec{p_2} = x_2\vec{P_2} \tag{4.4}$$

with the Bjorken scaling variable x_i. Since the hadrons (protons) and the partons (quarks and gluons) are considered massless, the relations from eq. 4.4 can be transferred to the energies, meaning

$$\begin{aligned} (p_1 + p_2)^\nu &= \Big(x_1E_{p_1} + x_2E_{p_2}, \underbrace{x_1\vec{P_1} + x_2\vec{P_2}}_{\vec{P_1}=-\vec{P_2}}\Big) \\ &= \Big((x_1 + x_2)E_{p_1}, (x_1 - x_2)\vec{P_1}\Big) \end{aligned} \tag{4.5}$$

in the HCMS.

The process of jet production in LO is described as a $2 \to 2$ parton scattering. The hadronic cross section is given by [12, p. 238]

$$\mathrm{d}\sigma = \sum_{i,j,k,l} \int \mathrm{d}x_1\, \mathrm{d}x_2\, f_i(x_1, \mu_f) f_j(x_2, \mu_f)\, \mathrm{d}\hat{\sigma}_{ij\to kl}, \tag{4.6}$$

where the cross section $\mathrm{d}\hat{\sigma}$ in the partonic subsystem was introduced (compare figure 7). It can be written as [4]

$$\mathrm{d}\hat{\sigma}_{ij\to kl} = \frac{1}{F}\overline{|M_{ij\to kl}|}^2 \mathrm{dPS}_n, \tag{4.7}$$

where F is the flux factor, M are the already calculated matrix elements and dPS_n is the Lorentz-invariant phase space volume. The cross section is influenced by the strong coupling constant α_s, causing it to depend on the renormalization scale μ_r. In eq. 4.6 the summation over identical initial ($i = j$) and final ($k = l$) states is excluded.

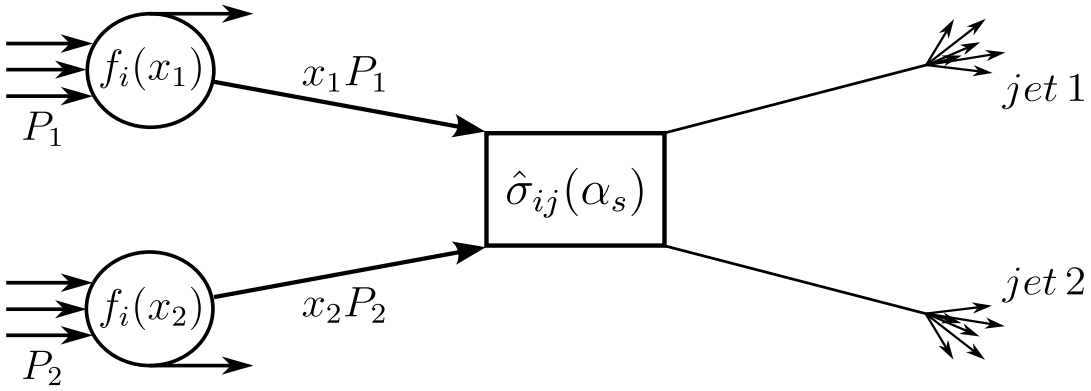

Figure 7: Schematic illustration of the collision of two hadrons.

In general, the phase space volume for a $n = 2$ particle final state is given as

$$\mathrm{dPS}(2\to 2) = \frac{\mathrm{d}^4k_1}{(2\pi)^3}\frac{\mathrm{d}^4k_2}{(2\pi)^3}\delta(k_1^2 - m_1^2)\delta(k_2^2 - m_2^2)(2\pi)^4\delta^{(4)}(p_1 + p_2 - k_1 - k_2). \tag{4.8}$$

Furthermore, the evaluation of the k^0-component reduces the 4-dimensional integration to a 3-dimensional integration

$$\begin{aligned}\frac{\mathrm{d}^4k}{(2\pi)^3}\delta(k^2 - m^2) &= \frac{\mathrm{d}^3\vec{k}}{(2\pi)^3}\frac{1}{2\sqrt{\vec{k}^2 + m^2}}\Big(\delta(k^0 - \sqrt{\vec{k}^2 + m^2})\mathrm{d}k^0 + \delta(k^0 + \sqrt{\vec{k}^2 + m^2})\mathrm{d}k^0\Big)\\ &= \frac{\mathrm{d}^3\vec{k}}{(2\pi)^3 2E}\theta(E),\end{aligned} \tag{4.9}$$

where the energy of the particle is set to a fixed value of $E = \sqrt{\vec{k}^2 + m^2}$.
Moreover, eq. 4.8 is simplified by using the delta function to eliminate the integration over x_1, x_2, k_2^x and k_2^y. Splitting it into four parts leads to

$$\begin{aligned}\delta^{(4)}(p_1 + p_2 - k_1 - k_2) = &\delta(-k_1^x - k_2^x)\delta(-k_1^y - k_2^y)\\ &\cdot\,\delta(x_1 P_{1,z} + x_2 P_{2,z} - k_1^z - k_2^z)\\ &\cdot\,\delta(x_1 E_{p_1} + x_2 E_{p_2} - E_1 - E_2).\end{aligned} \tag{4.10}$$

Note, that the particle fall along the z-axis and the momentum fragments along the other axes are omitted. The first two δ-functions will just set

$k_2^x = -k_1^x$ and $k_2^y = -k_1^y$.
Continuing with the δ-function in the second line, a relation between x_1 and x_2 can be established:

$$\begin{aligned} &\delta\left(\frac{\sqrt{s}}{2}(x_1 - x_2) - k_1^z - k_2^z\right) = \delta\left(\frac{\sqrt{s}}{2}(x_1 - x_2 - \frac{2(k_1^z + k_2^z)}{\sqrt{s}})\right) \\ &\Rightarrow x_1 = x_2 + \frac{2(k_1^z + k_2^z)}{\sqrt{s}}. \end{aligned} \tag{4.11}$$

This allows the last δ-function to be rewritten and set values for $x_{1/2}$:

$$\begin{aligned} &\delta\left(\frac{\sqrt{s}}{2}(x_1 + x_2) - E_1 - E_2\right) = \frac{1}{\sqrt{s}}\delta\left(x_2 + \frac{1}{\sqrt{s}}(k_1^z + k_2^z - E_1 - E_2)\right) \\ &\Rightarrow x_2 = \frac{E_1 + E_2}{\sqrt{s}} - \frac{k_1^z + k_2^z}{\sqrt{s}} \quad \text{and} \quad x_1 = \frac{E_1 + E_2}{\sqrt{s}} + \frac{k_1^z + k_2^z}{\sqrt{s}}. \end{aligned} \tag{4.12}$$

The goal is to express the momentum fractions by quantities, that are observed in the real accelerator experiment. Therefore, the rapidity

$$y_{1/2} = \frac{1}{2}\ln\left(\frac{E_{1/2} + k_{1/2}^z}{E_{1/2} - k_{1/2}^z}\right) \tag{4.13}$$

for the final state particles and the transverse momentum

$$k_T = \sqrt{(k_1^x)^2 + (k_1^y)^2} = \sqrt{(k_2^x)^2 + (k_2^y)^2} \tag{4.14}$$

are defined. In the $m \to 0$ limit, the rapidity aligns with the pseudorapidity stated in chapter 2.5, which depends on the angle from the beam direction.
For $x_{1/2}$ follows (see appendix A.3.1)

$$x_1 = \frac{k_T}{\sqrt{s}}(e^{y_1} + e^{y_2}) \quad \text{and} \quad x_2 = \frac{k_T}{\sqrt{s}}(e^{-y_1} + e^{-y_2}). \tag{4.15}$$

In order to convert the integral further into the appropriate observables, a coordinate transformation to polar coordinates with azimuth ϕ (angle of k_T in the (x, y)-plane) is carried out:

$$\mathrm{d}y_{1/2} = \frac{\mathrm{d}k_{1/2}^z}{E_{1/2}}, \qquad \mathrm{d}k_1^x \mathrm{d}k_1^y = k_T \mathrm{d}k_T \mathrm{d}\phi. \tag{4.16}$$

The detailed derivation is provided in appendix A.3.2.
Merging the results by applying the integration over the delta function and transitioning to the new variables leads to

$$\begin{aligned} &\int \mathrm{d}x_1 \mathrm{d}x_2 \mathrm{d}^3k_1 \mathrm{d}^3k_1 \frac{1}{E_1 E_2}\delta^{(4)}(p_1 + p_2 - k_1 - k_2) \\ &= \frac{2}{s}\frac{1}{E_1 E_2}\,\mathrm{d}k_1^x \mathrm{d}k_1^y \mathrm{d}k_1^z\,\mathrm{d}k_2^z \\ &= \frac{2}{s}\mathrm{d}y_1 \mathrm{d}y_2 k_T \mathrm{d}k_T \mathrm{d}\phi. \end{aligned} \tag{4.17}$$

The actual calculation of the matrix elements took place in the **parton center of mass system (PCMS)**, where the particles have the momenta

$$p_A = \begin{pmatrix} \frac{\sqrt{\hat{s}}}{2} \\ 0 \\ 0 \\ \frac{\sqrt{\hat{s}}}{2} \end{pmatrix}, \quad p_B = \begin{pmatrix} \frac{\sqrt{\hat{s}}}{2} \\ 0 \\ 0 \\ -\frac{\sqrt{\hat{s}}}{2} \end{pmatrix} \tag{4.18}$$

and the symbol '^' expresses the consideration in the PCMS. This system undergoes a boost relative to the HCMS along the z-axis with the velocity $\beta = \frac{(x_1 - x_2)}{(x_1 + x_2)}$ according to eq. 4.5.
The matrix elements in section 3 are expressed by the Mandelstam variables s, t, u. Since the calculation was performed at the partonic level, these variables must be substituted with $\hat{s}, \hat{t}, \hat{u}$.
The Lorentz-invariant scalar product sets up a relationship between the invariant masses $\sqrt{s}, \sqrt{\hat{s}}$ of the respective center of mass systems, which is then expressed in terms of the rapidities. With $p_A \cdot p_B = p_1 \cdot p_2$ follows

$$\hat{s} = x_1 x_2 s \overset{(4.15)}{=} k_T^2 (2 + e^{y_1 - y_2} + e^{-(y_1 - y_2)}) = 4 k_T^2 \cosh^2 \left(\frac{y_1 - y_2}{2} \right). \tag{4.19}$$

The matrix elements still depend on the Mandelstam variables. With the scattering

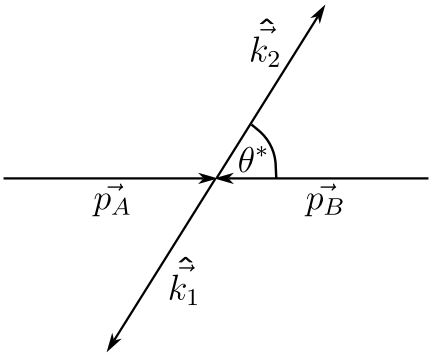

Figure 8: Scattering process in the partonic center of mass system and definition of the scattering angle θ^*. As in chapter 3, p_A and p_B correspond to the incoming partons.

angle θ^* in the PCMS (see fig. 8) the other variables can be expressed as

$$\hat{t} = -2 p_A \cdot \hat{k}_1 = -\frac{\hat{s}}{2} \big(1 - \cos(\theta^*) \big) \tag{4.20}$$

$$\hat{u} = -2 p_A \cdot \hat{k}_2 = -\frac{\hat{s}}{2} \big(1 + \cos(\theta^*) \big). \tag{4.21}$$

It is possible to link the scattering angle with the rapidities, thereby expressing all variables in terms of measurable observables (refer to appendix A.3.3):

$$\cos(\theta^*) = \tanh\big(\frac{y_1 - y_2}{2} \big). \tag{4.22}$$

With the flux factor

$$F = 4\sqrt{(p_A \cdot p_B)^2 - m_A^2 m_B^2} = 2\hat{s} \quad |m_i = 0, \tag{4.23}$$

the cross section will be independent of the number of particles contained in the beam. All in all it ensues with eq. 4.17 for the three differential cross section

$$\frac{\mathrm{d}^3\sigma}{\mathrm{d}k_T \mathrm{d}y_1 \mathrm{d}y_2} = \frac{k_T}{8\pi\hat{s}^2} \sum_{i,j,k,l} x_1 f_i(x_1, \mu_f) x_2 f_j(x_2, \mu_f) \overline{|M(\hat{s}, \hat{t}, \hat{u})|}^2_{ij\to kl}, \tag{4.24}$$

while the integrations over $\mathrm{d}\phi$ has led to a factor 2π.

The last step before calculating the actual cross section is to take a look at the physically allowed regions of y_1, y_2 and k_T, leading to the corresponding integration limits.
The fractions of momenta cannot exceed 100% of the proton's total momentum, implying that $x_{1,2} \leq 1$, which establishes the constraints for y_2:

$$\begin{aligned} x_1 &= \frac{k_T}{\sqrt{s}}(e^{y_1} + e^{y_2}) \leq 1 \\ \Leftrightarrow \quad y_2 &\leq \underbrace{\ln\left(\frac{\sqrt{s}}{k_T} - e^{y_1}\right)}_{y_{2,\max}(k_T, y_1)}, \\ x_2 &= \frac{k_T}{\sqrt{s}}(e^{-y_1} + e^{-y_2}) \leq 1 \\ \Leftrightarrow \quad y_2 &\geq \underbrace{-\ln\left(\frac{\sqrt{s}}{k_T} - e^{-y_1}\right)}_{y_{2,\min}(k_T, y_1)}. \end{aligned} \tag{4.25}$$

The integration limits of y_1 are bounded by the allowed region of y_2 (visualization in appendix A.3.4). From this follows the condition that

$$\begin{aligned} & y_{2,\min}(k_T, y_1) = y_{2,\max}(k_T, y_1) \\ \hookrightarrow \quad & -\operatorname{arcosh}\Big(\frac{\sqrt{s}}{2k_T}\Big) \leq \ y_1 \leq \operatorname{arcosh}\Big(\frac{\sqrt{s}}{2k_T}\Big). \end{aligned} \tag{4.26}$$

For k_T, the lower limit is $0 \leq k_T$. The argument of arcosh( ), which must be greater than 1, provides a condition for the upper limit of k_T:

$$k_T \leq \frac{\sqrt{s}}{2}. \tag{4.27}$$

Hence, the total cross section is determined by

$$\begin{aligned} \sigma = \sum_{i,j,k,l} \int_0^{k_{T,\max}} \mathrm{d}k_T \int_{y_{1,\min(k_T)}}^{y_{1,\max(k_T)}} \mathrm{d}y_1 \int_{y_{2,\min(k_T,y_1)}}^{y_{2,\max(k_T,y_1)}} \mathrm{d}y_2 \\ \cdot \frac{k_T}{8\pi\hat{s}^2} x_1 f_i(x_1, \mu_f) x_2 f_j(x_2, \mu_f) \overline{|M(\hat{s}, \hat{t}, \hat{u})|}^2_{ij\to kl}. \end{aligned} \tag{4.28}$$

5 Numerical Evaluation

In this chapter, the derived results will be validated through comparison with experimental data. Initially, the integration of eq. 4.24 was performed using the *scipy.integrate* Python library [21], but was subsequently switched to the *vegas* package [22], which employs an adaptive Monte Carlo vegas algorithm.
The set of parton distribution functions used is CT18NNLO [5]. From this set α_s is also provided. Due to the high mass of the top-quarks ($(171.77 \pm 0.37)\,\mathrm{GeV}$ [23]), their production will be neglected.

As a first step, the implemented numerics are checked against an external code (based on [24]), whereas the matrix elements have already been compared with [12, p. 249] and require no further checking. The process selected for the comparison is $q\bar{q} \to Q\bar{Q}$, where Q describes a fixed quark of a different flavor. In the limit where mass is negligible, the specific flavor of the final state quark Q does not matter.
The rapidity integration over y_2 was carried out within the limits specified in eq. 4.25, resulting in a confirmation for $\frac{\mathrm{d}\sigma^2}{\mathrm{d}y_1 \mathrm{d}k_T}$. Furthermore, agreements were also achieved for the y_1-integration with respect to the limits provided in eq. 4.26.
In addition to the estimated ratio between the code implemented in this work and the external code, a two-sample z-test is carried out

$$Z = \frac{\bar{X} - \bar{Y}}{\sqrt{\sigma_X^2 + \sigma_Y^2}}, \tag{5.1}$$

where $\bar{X}$ and $\bar{X}$ are the mean values of two different samples with respective standard error $\sigma_{\bar{X},\bar{Y}}$. The returned value is in units of standard deviations. A more detailed explanation of the comparison with the respective plots can be found in appendix A.4.

In the experiment, there is usually no access to an observable with a specific value, but rather to phase space bins of cross sections integrated over ranges and averaged over them. The computation of the fiducial cross section is therefore carried out over bins, but remains classified as a differential cross section by convention.
Before the comparison, it should be verified that changing the integration order of y_1 and y_2 does not affect the result, although they are related to different x-fractions. The integrated phase space and therefore the integration limits will remain unchanged, while the roles of x_1 and x_2 in the PDFs are swapped.
The proton-proton collision concludes only symmetric states, meaning the symmetry at the partonic level translates to the symmetry in rapidities of the two final states. This for example would be different for proton-lead collisions. To illustrate the breaking of symmetry for non-symmetric hadronic states, another PDF set (namely nCTEQ15 [25]) is used only for the second PDF (see f_j in eq. 4.6).
Figure 9 points out that by changing the integration order of y_1 and y_2, different values are calculated for the single differential cross section when using different parton distribution functions. This consequence does not occur with identical PDFs.

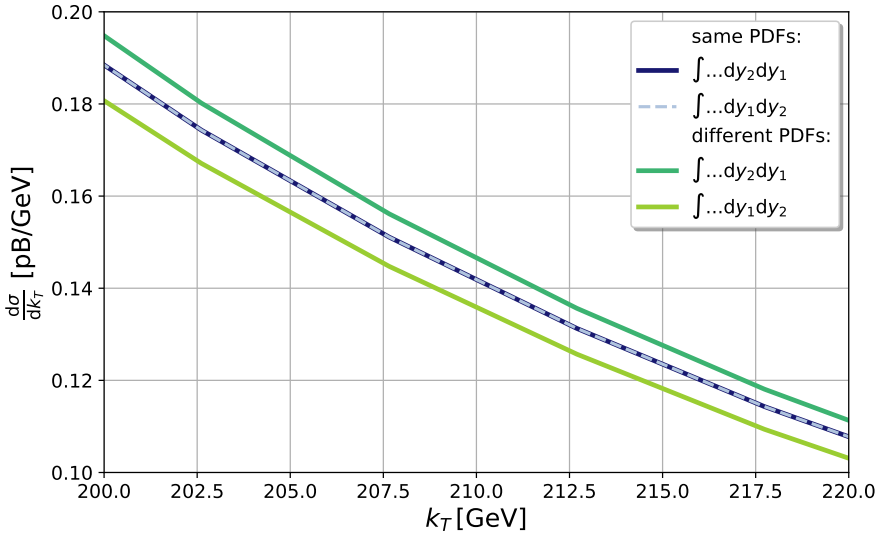

Figure 9: The integration of the single differential cross section is performed with same and different PDFs for the initial state particles, to emphasize that the order of integration over the rapidities is not trivial for non-symmetric states.

5.1 Share of Processes

To obtain an overview of the share of processes in jet production, figure 10 presents the single differential cross section integrated over the whole rapidity range. The processes are separated into color categories according to the particles in the initial state. It can be seen, that for $k_T < 500\,\text{GeV}$ the gluon-gluon scattering dominates,

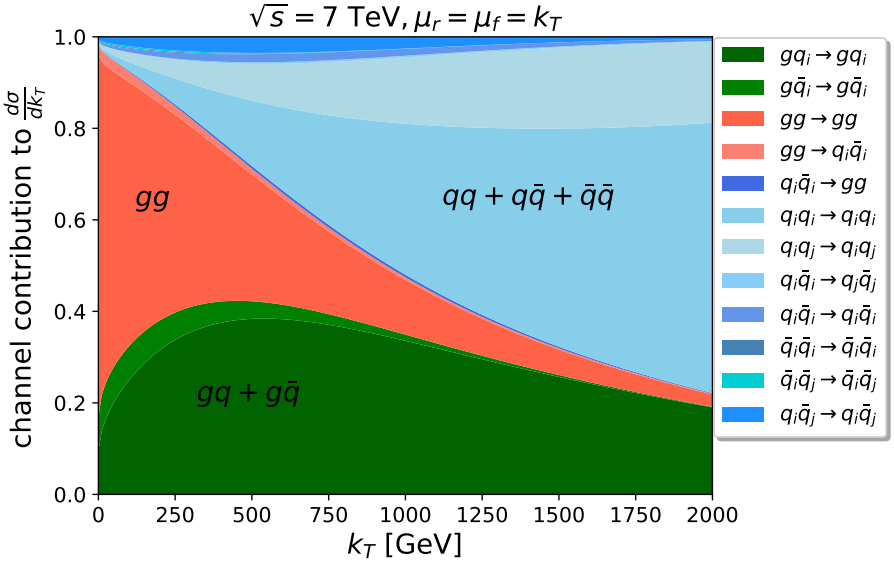

Figure 10: Share of the single differential cross section of the various processes with different parton combinations depending on the transverse momentum.

while processes containing only (anti)quarks have almost no fraction. For larger

transverse momenta the proportion changes, leading to a dominance of processes involving (anti)quarks. It is evident that gluon-quark interactions play an important role across all regions. This observation aligns with the PDFs presented in fig. 1, as there is a higher likelihood of encountering a low-momentum gluon, resulting more frequently in gluon-gluon interactions and to a lesser extent in gluon-quark fusion. In the blue area, the $q_i q_i \to q_i q_i$ and $q_i q_j \to q_i q_j$ processes are the most influential. The permanent presence of valence quarks within the proton causes increased annihilation involving quarks rather than antiquarks.

5.2 ATLAS Measurement

The measured inclusive jet cross section data in a proton-proton collision is provided by the ATLAS Collaboration [26]. This measurement was conducted with the ATLAS detector at the Large Hadron Collider at a center-of-mass energy of $\sqrt{s} = 7\,\text{TeV}$ using a data set corresponding to an integrated luminosity of $4.5\,\text{fb}^{-1}$. The double differential cross sections are shown as functions of jet transverse momentum and jet rapidity, covering jet transverse momenta from 100 GeV to 2 TeV and rapidities of $|y| \leq 3$. The measured jets identified by the anti-k_t algorithm [13] possess radii of $R_1 = 0.4$ and $R_2 = 0.6$, respectively. The renormalization scale and the factorization scale are set dynamically, depending on the phase space through the leading jet transverse momentum $\mu_r = \mu_f = k_T^{\max}$.
For comparison with the data, the cross section determined in this thesis is integrated over the whole y_2-range and then provided in bins of y_1 and k_T. In the subsequent plots, the $|y|$-values of the data are associated with the positive y_1-values.

5.2.1 Evaluation of Integration Methods

The integration carried out with SciPy was cross-checked with a Monte Carlo integration, where the code for calculation and iteration over the individual processes remained unchanged. The results could be reproduced for some channels and not for others, with no pattern emerging with regard to the particles involved. The

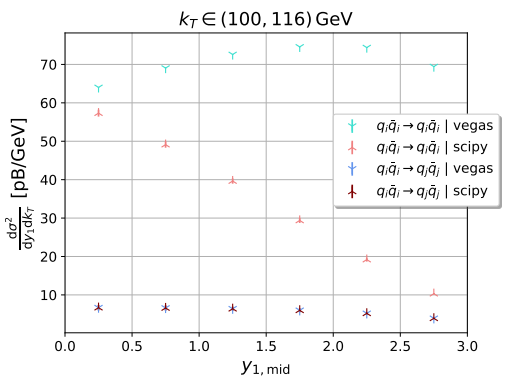

Figure 11: Cross section for $q_i\bar{q}_i \to q_i\bar{q}_i$ and $q_i\bar{q}_i \to q_j\bar{q}_j$ channels with comparison of different numerical integration methods.

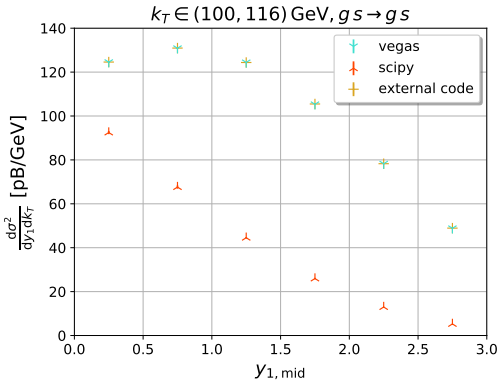

Figure 12: Comparison of different numerical integration methods with an external code for the $g\,s \to g\,s$ channel.

Figure 11 illustrates that the disagreement for the $q_i\bar{q}_i \to q_i\bar{q}_i$ process is well over the reported numerical errors. To verify which results are correct, a comparison is made with another code (based on [24]) for the $g\,s \to g\,s$ channel. In figure 12 the vegas result was confirmed, thus, the calculation with SciPy was discontinued. It was not attempted to precisely identify the source of this problem, so the calculation will henceforth be carried out using the vegas algorithm.

5.2.2 Uncertainties

There are three different types of uncertainties that have to be considered when performing the numerical calculation of the integral. An evaluation of the errors is shown in Figure 13 for the data, which is subsequently compared with the experimental data. The differential cross section is integrated in y_1-bins of width 0.5 for $k_T \in (100, 116)\,\text{GeV}$, where $y_{1,\text{mid}}$ denotes the middle of the respective bin.

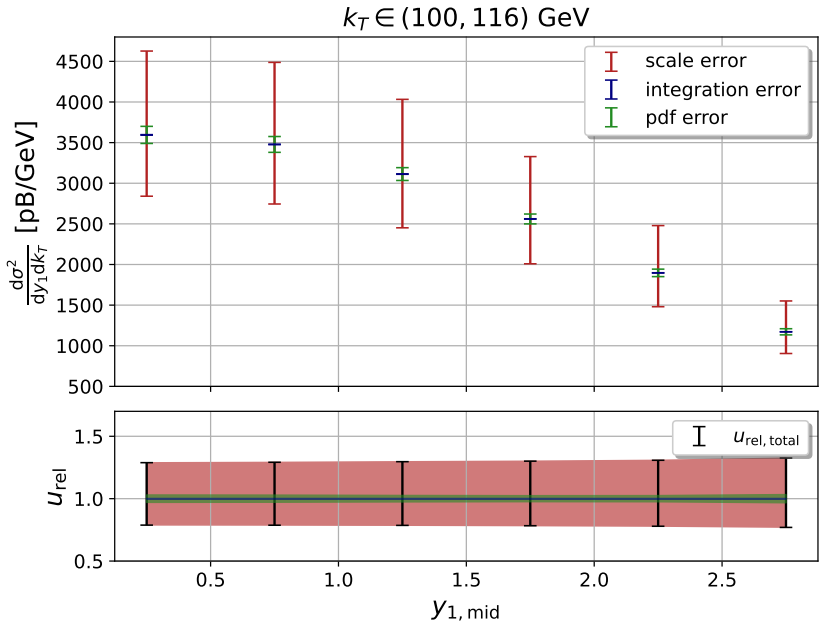

Figure 13: Theoretical prediction for jet production in leading order at $\sqrt{s} = 7\,\text{TeV}$ for $k_T \in (100, 116)\,\text{GeV}$. The three different sources of error are shown, with the scale error clearly dominating. The lower plot presents the relative uncertainties u_{rel}.

PDF uncertainty:
The used PDF set is together with the best estimate (central value) provided with 58 Hessian sets PFDs from which the uncertainty of an observable is determined. For observing the cross section, the uncertainty is given as

$$\Delta\sigma_{\text{pdf}} = \frac{1}{2}\sqrt{\sum_k \left(\sigma(f_k^+) - \sigma(f_k^-)\right)^2}. \tag{5.2}$$

The experimentally determined PDFs are fitted to the theoretical data by minimizing the χ^2 function. In its simplest form, it has the following structure for a single data

set

$$\chi_i^2(a_j) = \frac{[D_i - T_i(a_j)]^2}{\sigma_i'^2}. \tag{5.3}$$

Here, D_i are the experimental values, while T_i denote the theoretical predictions. The denominator $\sigma_i'^2 = \sigma_i^2 + u_i^2$ sums the statistical error σ_i and the uncorrelated systematic error u_i in quadrature. The χ^2 function is then minimized with respect to the fitting parameters a_j to find the best PDF, the *central value*.
The uncertainties can be quantified using the Hessian method, in which the χ^2-function is approximated near its minimum in a quadratic form:

$$\chi^2 = \chi_0^2 + \sum_{i,j} H_{ij}(a_i - a_i^0)(a_j - a_j^0) \quad |H_{ij} = \frac{1}{2}\Big(\frac{\partial^2 \chi^2}{\partial y_i \partial y_j}\Big), \tag{5.4}$$

where $y_i = (a_i - a_i^0)$ denotes the shifts from the actual minimum.
Finally, an upwards (f_k^+) and a downwards (f_k^-) error variation of the parameters is obtained, with which the central error is calculated according to equation 5.2. [25]
The relative PDF error is around 3% and is therefore in leading order significantly smaller than the error caused by the scale variation.

Scale uncertainty:
As discussed in section 2.4, the strong coupling constant α_s is a function of the chosen renormalization scale. Ideally, physical observables should not depend on the choice of scale, but this is not the case in LO. The dependence on the choice only disappears in case of an all-order calculation. However, the terms that explicitly depend on the renormalization scale will also have prefactors involving the coupling constant, implying that the impact of the choice of scale is reduced as more terms are added to the perturbative series.
Based on equation 2.28 the cross section is expected to decrease as the scale increases. The scale uncertainty is quantified by calculating the cross section on a scale of $\mu = 0.5 k_T^{\max}$ and $\mu = 2k_T^{\max}$ meaning

$$\Delta\sigma_{\text{scale}} = \left[\sigma\Big(2k_T^{\max}\Big), \sigma\Big(\frac{1}{2}k_T^{\max}\Big)\right], \tag{5.5}$$

which includes most of the possible variation.
The scale error is not symmetrical, but still exceeds the other errors in both directions. The relative error for $\mu = 2k_T^{\max}$ is about $u_{\text{rel},2k_T} \sim 20\%$ and for $\mu = \frac{1}{2}k_T^{\max}$ slightly greater with $u_{\text{rel},0.5k_T} \sim 30\%$.

Integration error:
The error resulting from the numerical integration is of a much lower order of magnitude compared to the scale and PDF uncertainty. By computing the cross section using the vegas algorithm, the uncertainty can be reduced as much as desired by increasing the number of integral evaluations.
The total uncertainty is calculated by

$$\Delta\sigma = \sqrt{\Delta\sigma_{\text{pdf}}^2 + \Delta\sigma_{\text{scale}}^2 + \Delta\sigma_{\text{int}}^2}. \tag{5.6}$$

5.2.3 Comparison to Data

At first, the theoretical calculation in LO is compared to the ATLAS data at a fixed k_T range with y_1-bins varied from $0 \leq y_1 \leq 3$ with a width of $y_{\text{width}} = 0.5$.
Figure 14a shows the comparison for k_T in a range from 100 GeV to 116 GeV. For the smaller radius of $R_1 = 0.4$ the results align with the calculations within the error bars for all $y_{1,\text{mid}}$-values. Consequently, the Z-value lies between $Z_{R_1} = \pm 1\sigma$. It is evident that the agreement is worse for the smaller rapidity bin ranges, while in ranges $1.5 \leq y_1 \leq 2$ and $2 \leq y_1 \leq 2.5$ the best agreement is reached.

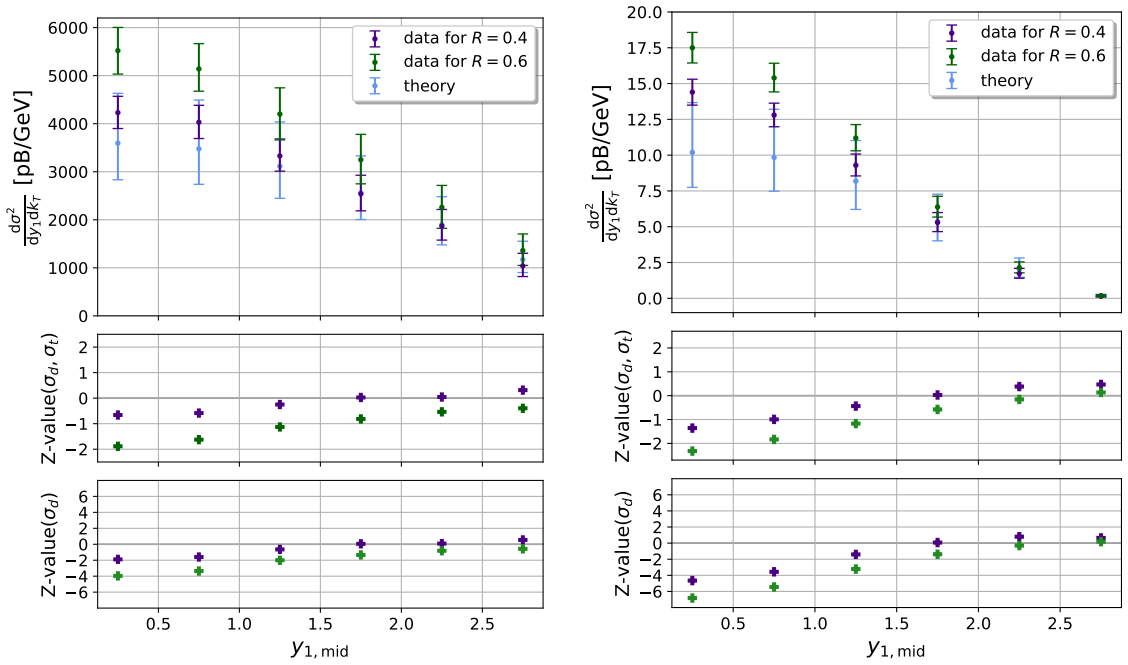

(a) $k_T \in (100, 116)$ GeV (b) $k_T \in (290, 318)$ GeV

Figure 14: Theoretical prediction for the cross section in bins of k_T and y_1 in proton-proton collision in leading order compared the experimental data at $\sqrt{s} = 7$ TeV. The k_T range is kept constant.

When considering the radius $R_2 = 0.6$, the agreement decreases ($Z_{R_2} = \pm 2\sigma$). For experimental points in $0 \leq y_1 \leq 0.5$ and $0.5 \leq y_1 \leq 1$, the error bars do not overlap. The consideration of two different radii leads to the assumption that in the (unphysical) limit $R \to 0$ the agreement increases.
The plots also provide the Z-value without taking the error of the theoretical prediction σ_t into account. As the scale variation error is no longer included in the comparison, only an agreement of order 2σ (R_1) and 4σ (R_2) is achieved.
Figure 14b displays the data for $k_T \in (290, 318)$ GeV. The discrepancy is larger when compared to the data for lower transverse momenta, placing the Z-Value for R_1 within $Z_{R_1} = \pm 1.5\sigma$ and for R_2 within $Z_{R_2} = \pm 2.5\sigma$.
It is apparent that the majority of the cross section is produced in the region where k_T is low and y_1 approaches zero. At higher k_T-values, the collisions involve particles carrying a greater fraction of the proton's momentum (see section 5.3). Observing

the PDFs in fig. 1, it becomes clear that the likelihood of finding such high-x particles is reduced. Moreover, eq. 4.24 indicates that the differential cross section is inversely proportional to k_T when applying eqs. 4.15 and 4.19.

In addition, the cross section was calculated for fixed y_1-ranges with varying transverse momentum. Due to the restriction in eq. 4.26, the maximum y_1-value for a given interval decreases with increasing k_T. The comparison with the experimental data for three distinct y_1-bins is presented in fig. 15a. The Z-value indicates that the deviation is larger within the $0 \leq y_1 \leq 0.5$ range, which corresponds to the region where the share of the total cross section is greatest compared to the larger y_1-areas. As visualized in fig. 15b, which shows the ratio between prediction and data, the experimental results lie within the uncertainty bands for the two intervals with higher y_1-values. For the $0 \leq y_1 \leq 0.5$ range, there is only an agreement for small values of $k_T < 172\,\text{GeV}$.

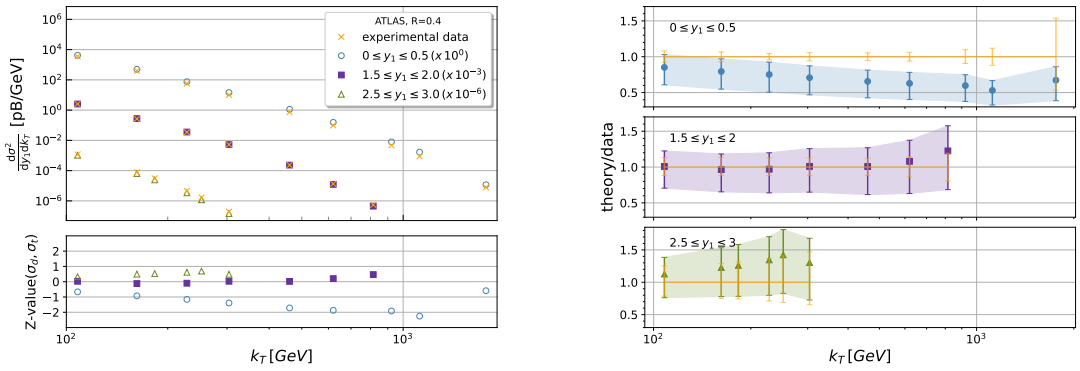

(a) (b)

Figure 15: Theoretical prediction for the cross section in pp-collision in leading order for different k_T-bins in a varying y_1-range (left). The right-hand plot depicts the uncertainties and ratios; bands represent the scaled prediction errors, while the bars show the experimental data errors.

When the uncertainties are taken into account, the overall agreement can be considered positive, as all calculated results are of a similar magnitude to those obtained by the ATLAS detector. It is important to emphasize that this is merely a leading order calculation, where the hard partons correspond to the upcoming jets. Processes such as gluon emission in the final state and thus 3-jet events, for example, are not included. This limitation also implies that the jet radius R is not incorporated into the theoretical model.
Furthermore, the experimental data is presented in bins of absolute values of y, while the model provided in this thesis integrates over the whole y_2 phase space and takes only the positive y_1-values into account.
The approximation that the quarks are assumed to be massless should have no noticeable influence on the calculation for the transverse momenta ($k_T > 100\,\text{GeV}$) considered here.
For more in-depth investigations, a calculation in higher orders is recommended.

5.3 Sensitive Kinematic Region

The x-region, which is most sensitive to the cross section, will be the subject of the further analysis. Therefore, the double differential cross section at $\sqrt{s} = 7\,\text{TeV}$ is calculated in 99 bins between $0 \leq x_1 \leq 1$ and compared to the naive expectation in leading order, where the relationship is given by eq. 4.15. This is shown in figure 16

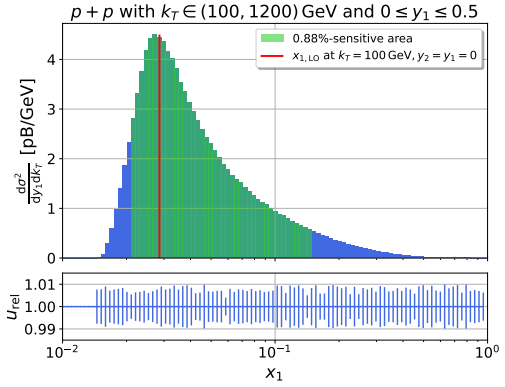

Figure 16: Sensitive x_1-region for $0 \leq y_1 \leq 0.5$ at $k_T \in (100, 1200)\,\text{GeV}$ compared to the expectation in LO.

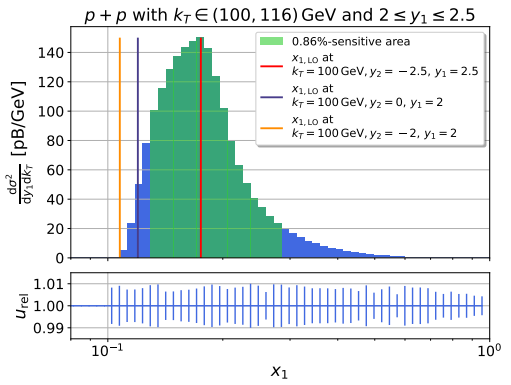

Figure 18: Sensitive x_1-region for $2 \leq y_1 \leq 2.5$ at $k_T \in (100, 116)\,\text{GeV}$ compared to the expectation in LO.

for a range of $k_T \in (100, 1200)\,\text{GeV}$ in the lowest positive rapidity bin of y_1, where the green bars indicate the range of x_1 that contributes $\sim 90\%$ to the cross section. Starting from the edge of the distribution, a 5% contribution to the cross section was omitted from both sides to obtain the green area. Due to the non-infinitesimal bin width, the 90%-value cannot always be fully reached. The Monte Carlo integration was performed in such a way that any evaluation was discarded if the current x-sample was not within the specified x-range. In the region of the peak, 30,000 evaluations per iteration of the Monte Carlo integration were performed, while for the other regions the number of evaluation was based on the relative uncertainty u_{rel} remaining below 1%.

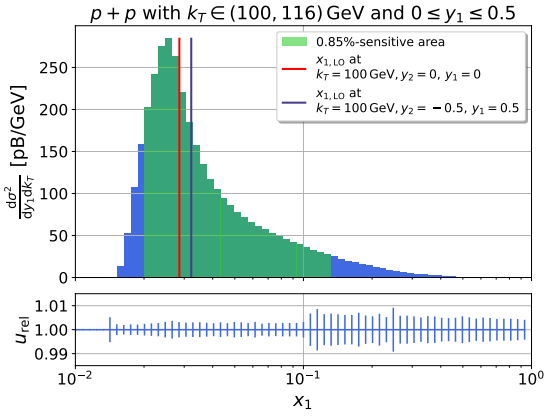

(a) $k_T \in (100, 116)\,\text{GeV}$

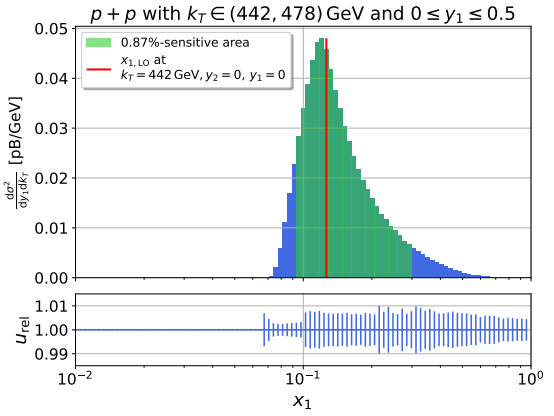

(b) $k_T \in (442, 478)\,\text{GeV}$

Figure 17: Sensitive x_1-region for $0 \leq y_1 \leq 0.5$ at different k_T-ranges compared to the expectation in LO.

It is observed that the calculation agrees well with the expectation in LO for $k_T = 100\,\text{GeV}$ and $y_1 = y_2 = 0$. The determined bin that is most sensitive to the cross section is $x_{1,\text{max}} = [0.027, 0.031]$.
In a narrower k_T range, the regions with larger k_T are associated with higher x_1-values (fig. 17b, $x_{1,\text{max}} = [0.118, 0.123]$), in contrast to regions with smaller momentum (fig. 17a, $x_{\text{max}} = [0.085, 0.089]$). As stated in section 5.2.3, the contribution to the total cross section is much greater in areas of lower k_T. Figure 17a also provides the LO expectation for the upper limit of the bin ($y_1 = 0.5$). The discrepancy is worse in this case, which could be due to the fact that rapidity distributions typically have a peak at $y = 0$ (see [27], fig. 11).

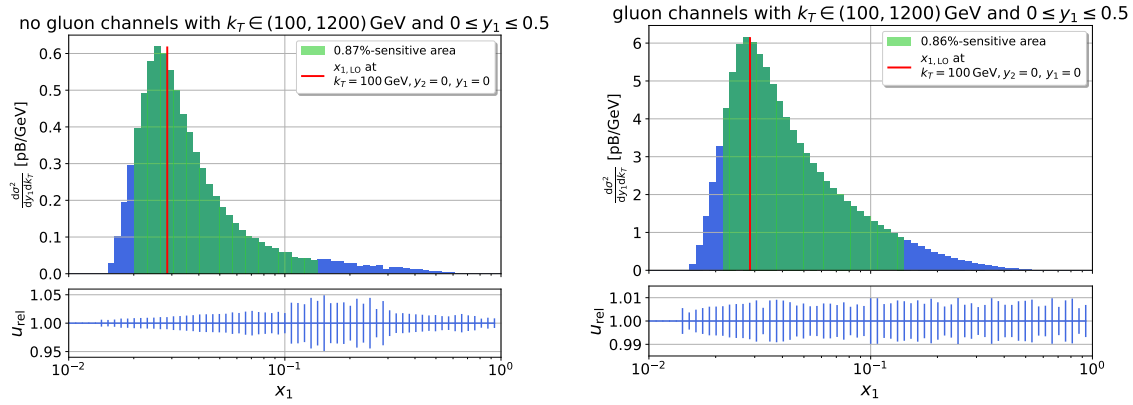

(a) (b)

Figure 19: Sensitive x_1-region for channels, which contain (no) gluon interaction, in pp-collision for $k_T \in (100, 1200)\,\text{GeV}$ and $0 \leq y_1 \leq 0.5$.

For higher rapidity data as in figure 18 the agreement is only valid for choosing the upper edge of the y_1 bin, while this was not the case for the smaller rapidity range. In LO, the momenta of the outgoing particles are back to back, so that $y_2 = -y_1$ is chosen, what agrees with the calculation. However, if a lower rapidity value from the bin interval is chosen, this agreement no longer holds, as illustrated by the orange line in figure 18. When larger rapidities are considered, the peak shifts to higher x. The share of the cross section of processes contributing gluons is approximately 10-times larger than for channels without gluons (see fig. 19), while the peak position remains roughly unchanged.

As a further step, the sensitive region for the factorization scale μ_f (which will be associated with the momentum transfer Q^2 here) can be determined, which is set to k_T in the computation. The analysis shows that the lowest momentum within a bin is leading, thereby causing the effective cross section's proportion to decrease as Q increases (fig. 20a). This holds true for any chosen momentum or rapidity interval, as demonstrated in fig. 20b, where the distribution for $2.5 \leq y_1 \leq 3$ at $k_T \in (290, 318)\,\text{GeV}$ is presented.

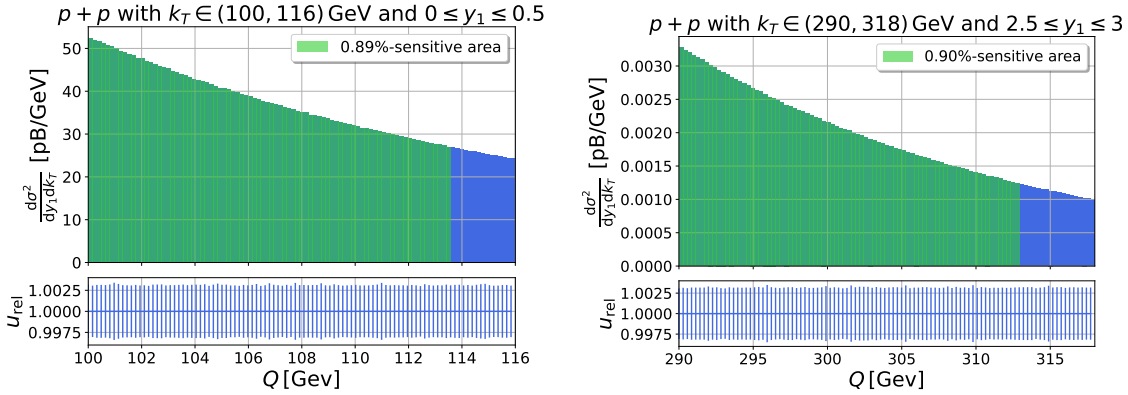

(a) $0 \leq y_1 \leq 0.5$ at $k_T \in (100, 116)$ GeV. (b) $2.5 \leq y_1 \leq 3$ at $k_T \in (290, 318)$ GeV.

Figure 20: Sensitive Q-region for selected y_1- and k_T-bins with relative uncertainty u_{rel}.

Finally, figure 21 illustrates the kinematic reach of the jet production for the experimental points of figure 17 in the (x, Q^2)-plane. The uncertainties are given by the specified sensitive ranges, normalized to 90%. It is clear to see that the measuring

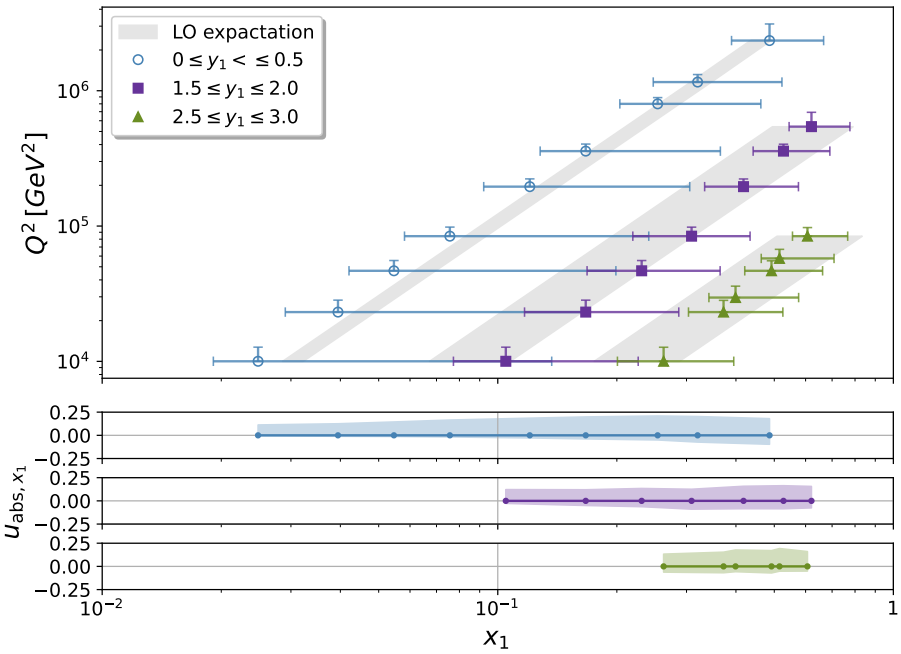

Figure 21: Calculated kinematic reach of the jet production at leading order at $\sqrt{s} = 7\,\text{TeV}$. The error bars indicate the region, which is 90% sensitive to the double differential cross section. To indicate the width of the green area in the previous plots, this plot also provides the absolute uncertainty of $x_{1,\text{max}}$ separately.

of high rapidity, what corresponds to small detecting angles, results from particles scattering with a high share of the proton's momentum. On a double logarithmic

scale, the relationship between x_1 and Q^2 appears to be approximately linear. This means that within a bin, the highest momentum transfer Q^2 is associated with the highest x_1 value.
When examining the absolute uncertainties u_{abs,x_1} of $x_{1,\text{max}}$ (width of the green area, i.e. the sharpness of the peaks) resulting from the sensitive regions, there is no clear correlation between x_1 and k_T respective y_1. Nevertheless, it is apparent that the majority of the cross section is produced by x_1, which are greater than $x_{1,\text{max}}$.
The naive expectation in LO is shown within the gray boxes, with the lower limit of each rapidity bin selected as the left bound and the upper limit as the right bound, under the condition that $y_2 = -y_1$. Almost all x_1-peak positions are within these boxes, only for the $0 \leq y_1 \leq 0.5$ range there are slight deviations for small Q^2.
It should be emphasized that the inclusion of the 90% sensitive region (regarding the cross section) instead of the most sensitive point covers a significantly larger area.
For higher orders, the assumption that the jets must necessarily be back-to-back becomes invalid. Further analysis could provide insight into whether the computational order substantially influences the results.

6 Conclusion

This work started with the analytical determination of the three differential cross section in LO for selected processes in proton-proton collision, namely $qq \to qq$, $q\bar{q} \to q\bar{q}$, $\bar{q}\bar{q} \to \bar{q}\bar{q}$ and $gg \to gg$. The results were integrated by an adaptive Monte Carlo algorithm with the *vegas* [22] package in Python.
First, the contribution of the various channels to the single differential cross section $\frac{d\sigma}{dk_T}$ in a range of $k_T \in (0, 2000)\,\text{GeV}$ was analyzed. It was determined that the $gg \to gg$ process dominates for transverse momenta $k_T < 500\,\text{GeV}$, while quark and antiquark interactions play a major role for $k_T > 500\,\text{GeV}$. Gluon-antiquark interactions have a share of at least one fifth of the cross section, regardless of k_T.

The calculated double differential cross section, which was integrated over the whole y_2-range and in bins of k_T and y_1, was compared with an ATLAS detector measurement at the LHC in proton-proton collisions at $\sqrt{s} = 7\,\text{TeV}$, which provided data for jet radii of $R_1 = 0.4$ and $R_2 = 0.6$.
In a fixed range of $k_T \in (100, 116)\,\text{GeV}$ with varying y_1-bins of width 0.5 the calculation aligned well with the ATLAS R_1-data within error bars for all y_1 values, with an agreement of the order 1σ. For R_2 the correlation diminishes and is of the order 2σ.
Considering a range with larger momenta $k_T \in (290, 318)\,\text{GeV}$, it was observed that the proportion of the total cross section decreases markedly. In this range, worse agreements were achieved, which are nevertheless satisfactory for the LO calculation.
A limitation of the theoretical model is the exclusion of the jet radius in the LO calculation results. Including data with smaller radii could enhance the comparison. In addition, the $|y|$-dependence of the results could be investigated further, since in this thesis the cross section was only integrated over the positive y_1 ranges.

The examination of the x-region, which is most sensitive to the cross section, showed that the results match with the explicit LO expectation. It was found that areas with larger transverse momentum k_T as well as areas with larger y_1 are associated with larger x-values.
The investigation of the sensitivity of the factorization scale, set to the leading transverse momentum of a bin, revealed that the lowest k_T value contributes the most to the cross section. The kinematic reach of the jet production could be illustrated in the (x, Q^2)-plane, whereby the inclusion of the 90% cross section sensitivity of x and Q provided significantly greater coverage in the plane. A next-to-leading order calculation would not only be interesting to reduce the scale dependency in the first part, but would also be useful for a more comprehensive examination of the sensitive region to see whether differences to the LO approximation occur.

A Appendix

A.1 Dirac Matrices

The $4x4$ matrix $\not{k}$ is defined as

$$\not{k} \equiv k_\mu \gamma^\mu$$

for a four-vector k^μ.
The Dirac matrices are defined as unitary and traceless 4×4 matrices

$$\gamma^0 \equiv \begin{pmatrix} 1 & 0 \\ 0 & -1 \end{pmatrix}, \quad \gamma^i = \begin{pmatrix} 0 & \sigma^i \\ -\sigma^i & 0 \end{pmatrix}, \tag{A.1}$$

where σ^i are the Pauli matrices. The relations are taken from [6]
General relations:

$$\{\gamma^\mu, \gamma^\nu\} = 2g^{\mu\nu} \tag{A.2}$$

$$(\gamma^\mu)^\dagger = \gamma^0 \gamma^\mu \gamma^0 \tag{A.3}$$

Product rules:

$$\gamma_\mu \gamma^\mu = 4 \tag{A.4}$$

$$\gamma_\mu \gamma^\nu \gamma^\mu = -2\gamma^\nu \tag{A.5}$$

$$\gamma_\mu \gamma^\nu \gamma^\rho \gamma^\mu = 4g^{\nu\rho} \tag{A.6}$$

$$\gamma_\mu \gamma^\nu \gamma^\sigma \gamma^\rho \gamma^\mu = -2\gamma^\rho \gamma^\sigma \gamma^\nu \tag{A.7}$$

Trace theorems:

$$\begin{aligned} \mathrm{Tr}(\gamma^\mu \gamma^\nu) &= 4g^{\mu\nu} \\ \mathrm{Tr}(\gamma^\mu \gamma^\nu \gamma^\lambda \gamma^\sigma) &= 4(g^{\mu\nu} g^{\lambda\sigma} - g^{\mu\lambda} g^{\nu\sigma} + g^{\mu\sigma} g^{\nu\lambda}) \end{aligned} \tag{A.8}$$

The product of an odd number of gamma matrices always equals zero.

A.2 Mandelstam Variables

The Lorentz-invariant Mandelstam variables are defined as

$$\begin{aligned} s &= (p_\mathrm{A} + p_\mathrm{B})^2 = (k_1 + k_2)^2 \\ t &= (p_\mathrm{A} - k_1)^2 = (p_\mathrm{B} - k_2)^2 \\ u &= (p_\mathrm{A} - k_2)^2 = (p_\mathrm{B} - k_1)^2. \end{aligned} \tag{A.9}$$

They are not independent from each other

$$s + t + u = m_\mathrm{A}^2 + m_\mathrm{B}^2 + m_1^2 + m_2^2. \tag{A.10}$$

Considering massless particles, they fulfill

$$(p_A \cdot p_B) = (k_1 \cdot k_2) = \frac{1}{2}s \tag{A.11}$$

$$(p_A \cdot k_1) = (p_B \cdot k_2) = -\frac{1}{2}t \tag{A.12}$$

$$(p_A \cdot k_2) = (p_B \cdot k_1) = -\frac{1}{2}u. \tag{A.13}$$

A.3 Kinematics

A.3.1 Momentum Fractions

Starting with eq. 4.13 one can obtain

$$e^{\pm y_1} = \sqrt{\frac{E_1 \pm k_1^z}{E_1 \mp k_1^z}} = \sqrt{\frac{(E_1 \pm k_1^z)(E_1 \pm k_1^z)}{(E_1 \mp k_1^z)(E_1 \pm k_1^z)}} = \sqrt{\frac{(E_1 \pm k_1^z)^2}{E_1^2 - {k_1^z}^2}} = \frac{(E_1 \pm k_1^z)}{k_T}. \quad \text{(A.14)}$$

Analogously follows:

$$e^{\pm y_2} = \frac{(E_2 \pm k_2^z)}{k_T}. \quad \text{(A.15)}$$

So in total the momentum fractions (eq. 4.12) can be expressed through the rapidities:

$$x_1 = \frac{k_T}{\sqrt{s}}(e^{y_1} + e^{y_2}) \quad \& \quad x_2 = \frac{k_T}{\sqrt{s}}(e^{-y_1} + e^{-y_2}). \quad \text{(A.16)}$$

A.3.2 Coordinate Transformation

The goal is to express the rapidity via the energy and the momentum in z-direction. Therefore, the total differential can be calculated:

$$\begin{aligned} \mathrm{d}y &= \frac{\partial y}{\partial k}\mathrm{d}k + \frac{\partial y}{\partial E}\mathrm{d}E \\ \Rightarrow \frac{\mathrm{d}y}{\mathrm{d}k} &= \frac{\partial y}{\partial k} + \frac{\partial y}{\partial E}\frac{\partial E}{\partial k}, \end{aligned} \quad \text{(A.17)}$$

where

$$\begin{aligned} \frac{\partial y}{\partial k} &= \frac{1}{2}\frac{E_1 - k_1^z}{E_1 + k_1^z} \cdot \frac{(E_1 - k_1^z) + (E_1 + k_1^z)}{(E_1 - k_1^z)^2} \\ &= \frac{E_1}{E_1^2 - {k_1^z}^2} \end{aligned} \quad \text{(A.18)}$$

and

$$\begin{aligned} \frac{\partial y}{\partial E}\frac{\partial E}{\partial k} &= \frac{1}{2}\frac{E_1 - k_1^z}{E_1 + k_1^z} \cdot \frac{(E_1 - k_1^z) - (E_1 + k_1^z)}{(E_1 - k_1^z)^2} \cdot \frac{k_z}{E_1} \\ &= -\frac{{k_1^z}^2}{E_1({E_1^z}^2 - {k_1^z}^2)}. \end{aligned} \quad \text{(A.19)}$$

Merging the results gives

$$\frac{\mathrm{d}y_1}{\mathrm{d}k_1^z} = \frac{1}{E_1}, \quad \text{(A.20)}$$

while the same applies for y_2 and E_2.
Finally, polar coordinates are used, whereby the momentum is parameterized as follows [12, p. 246]

$$k^\mu = \begin{pmatrix} E_T \cosh y \\ k_T \sin\phi \\ k_T \cos\phi \\ E_T \sinh y \end{pmatrix}, \quad \text{(A.21)}$$

with the azimuthal angle ϕ.
This leads to the Jacobian determinant $|\frac{\partial(k_1^x,k_1^y)}{\partial(k_T,\phi)}| = k_T$ so in total:

$$\mathrm{d}k_1^x \mathrm{d}k_1^y = k_T \mathrm{d}k_T \mathrm{d}\phi. \tag{A.22}$$

A.3.3 Rapidity

To express the scattering angle θ^* by the rapidities of the outgoing partons, the differences in the hadronic and partonic CMS should be considered. The actual observed rapidities of the jets in the hadronic frame contain a boost, meaning

$$y_{1,2} = y_{\mathrm{PCMS}} \pm \hat{y}, \tag{A.23}$$

where $y_{\mathrm{PCMS}} = \frac{1}{2}(y_1 + y_2)$ is the laboratory rapidity and $\hat{y} = \frac{1}{2}(y_1 - y_2)$ are the final rapidities in the two-parton system.

Furthermore, θ^* can be written as

$$\cos(\theta^*) = \frac{\hat{k_z}}{|\hat{k}|} \tag{A.24}$$

using

$$e^{\hat{y}} \pm e^{-\hat{y}} = \begin{cases} \frac{2\hat{E}}{\sqrt{(\hat{E}-\hat{k_z})(\hat{E}+\hat{k_z})}} & \text{for } + \\ \frac{2\hat{k_z}}{\sqrt{(\hat{E}-\hat{k_z})(\hat{E}+\hat{k_z})}} & \text{for } - \end{cases} \tag{A.25}$$

what follows from eq. A.14, we can express the angle as

$$\cos(\theta^*) = \frac{\hat{k_z}}{\hat{E}} = \frac{\hat{k_z} \cdot \left(\frac{2}{\sqrt{(\hat{E}-\hat{k_z})(\hat{E}+\hat{k_z})}}\right)}{\hat{E} \cdot \left(\frac{2}{\sqrt{(\hat{E}-\hat{k_z})(\hat{E}+\hat{k_z})}}\right)} = \frac{e^{\hat{y}} - e^{-\hat{y}}}{e^{\hat{y}} + e^{-\hat{y}}} = \tanh\left(\frac{y_1 - y_2}{2}\right). \tag{A.26}$$

A.3.4 Integration Limits

Figure 22 represents the intersection of $y_{2,\min}$ and $y_{2,\max}$, from which the limits of y_1 are derived. The solid line shows values for y_1 in the range

$$y_1 \in \left[-\operatorname{arcosh}\left(\frac{\sqrt{s}}{2k_T}\right), \operatorname{arcosh}\left(\frac{\sqrt{s}}{2k_T}\right)\right] \tag{A.27}$$

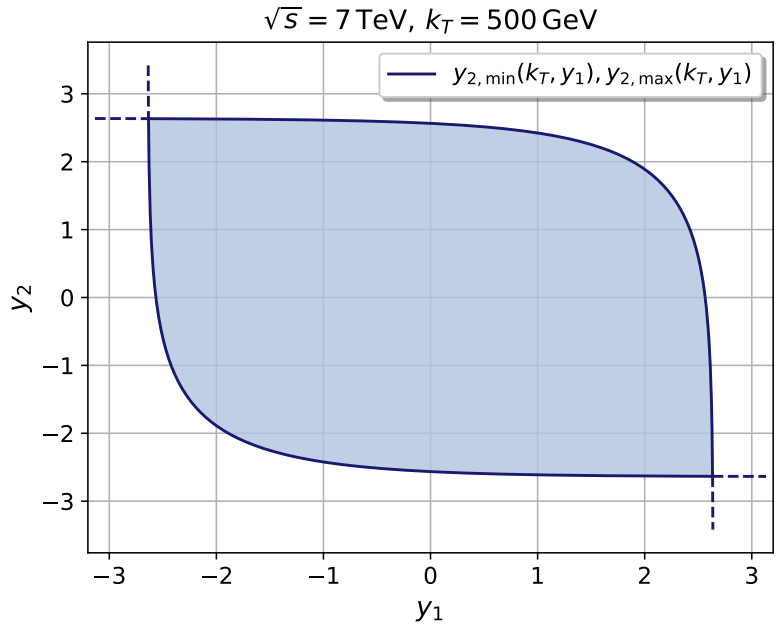

Figure 22: Visualization of the integration region for the single differential cross section $\mathrm{d}\sigma/\mathrm{d}k_T$. The solid lines represent the limits calculated in eqs. 4.26 and 4.25.

A.4 Validation of the Numerics

As this part is only a validation of the code without a physical background, the renormalization and factorization scale are arbitrarily set to $\mu_f = \mu_r = Q = 50\,\text{GeV}$. The center-of-mass energy of the system is set to $\sqrt{s} = 13\,\text{TeV}$, whereas the transverse momentum is in a range $k_T \in (0, 500)\,\text{GeV}$. Moreover, the ratio is defined as $\text{ratio} = \frac{\text{code}_{\text{thesis}}}{\text{code}_{\text{external}}}$.

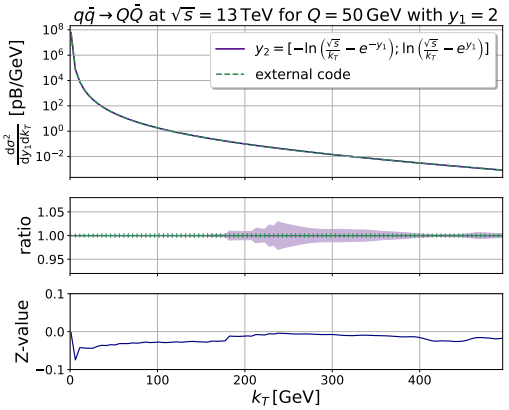

Figure 23: Double differential cross section $\frac{\mathrm{d}\sigma^2}{\mathrm{d}y_1 \mathrm{d}k_T}$ for a fixed value of $y_1 = 2$ in $k_T \in (0, 500)\,\text{GeV}$.

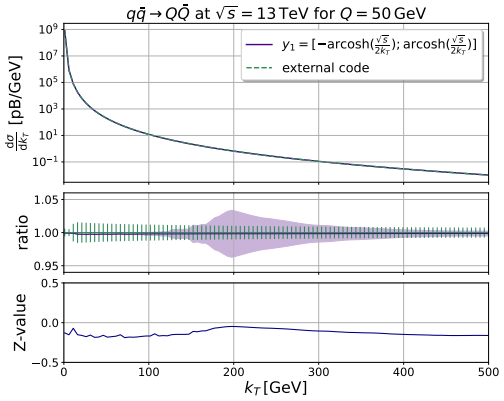

Figure 24: Single differential cross section $\frac{\mathrm{d}\sigma}{\mathrm{d}k_T}$.

The integration uncertainties are displayed in the ratio plots. Therefore, a curve with all values equal to one, along with error bars representing the relative uncertainties

of the external code, is shown. The ratio is provided with error bands indicating the scale variation error, meaning the relative uncertainties of the integration performed in this thesis are multiplied by the ratio.
The figures 23 and 24 show a satisfactory agreement between the codes. The differential cross section is integrated in a binned region for a width $k_{T,\text{width}} = 50\,\text{GeV}$ in fig. 25. There is a deviation in the region of small momenta, but for the subsequent calculation only calculation for momenta greater than $k_T = 100\,\text{GeV}$ are relevant.
The cross section is also integrated in a range $k_T \in (100, 116)\,\text{GeV}$ with y_1 binned from $0 \leq y_1 \leq 3$ in steps of width 0.5 (fig. 26).

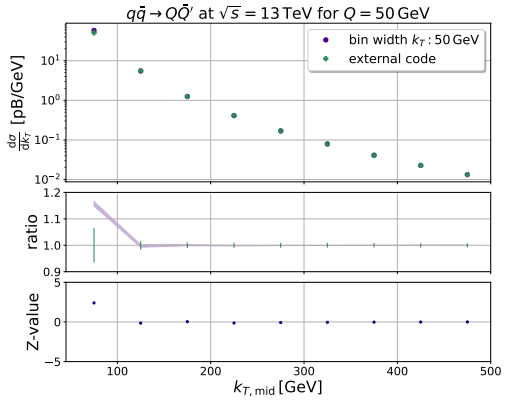

Figure 25: Cross section with k_T integrated in phase space bins with a width of 50 GeV. For small momenta, the integration with *scipy.integrate* is not stable.

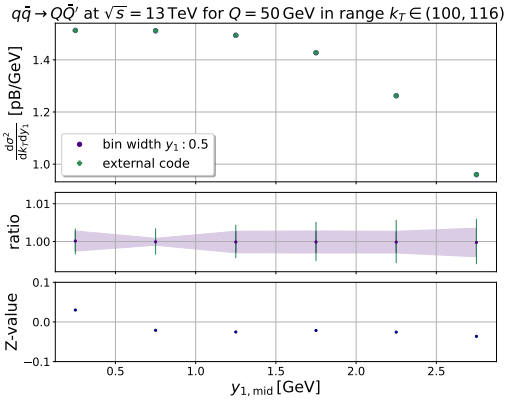

Figure 26: Cross section with k_T integrated in a range $k_T \in (100, 116)\,\text{GeV}$ with y_1 binned from $0 \leq y_1 \leq 3$ in steps of width 0.5.

References

[1] Söding, P. "On the discovery of the gluon". In: *Eur. Phys. J. H* 35.1 (2010), pp. 3–28. DOI: 10.1140/epjh/e2010-00002-5. URL: https://doi.org/10.1140/epjh/e2010-00002-5.

[2] A. Ali and G. Kramer. "JETS and QCD: a historical review of the discovery of the quark and gluon jets and its impact on QCD". In: *The European Physical Journal H* 36.2 (Sept. 2011), pp. 245–326. ISSN: 2102-6467. DOI: 10.1140/epjh/e2011-10047-1. URL: http://dx.doi.org/10.1140/epjh/e2011-10047-1.

[3] Bogdan Povh et al. *Particles and Nuclei*. 6th ed. Berlin, Germany: Springer, 2008.

[4] Alan D. Martin Francis Halzen. *Quarks and Leptons: An Introductory Course in Modern Particle Physics*. John Wiley & Sons, Inc., 1984.

[5] Tie-Jiun Hou et. al. *Progress in the CTEQ-TEA NNLO global QCD analysis*. 2019. arXiv: 1908.11394 [hep-ph].

[6] David Griffiths. *Introduction to Elementary Particles*. 2nd ed. Weinheim: WILEY-VCH Verlag GMbH & Co. KGaA, 2008.

[7] Benjamin Grinstein. "Introductory lectures on QCD". In: *2nd CERN-CLAF School of High Energy Physics*. June 2003, pp. 27–56.

[8] Howard E. Haber. "Useful relations among the generators in the defining and adjoint representations of SU(N)". In: *SciPost Phys. Lect. Notes* (2021), p. 21. DOI: 10.21468/SciPostPhysLectNotes.21. URL: https://scipost.org/10.21468/SciPostPhysLectNotes.21.

[9] S. Bethke, G. Dissertori, and G. Salam. "Quantum Chromodynamics". In: *Chin. Phys. C* 38 (2014). Ed. by K. A. Olive et al. (Particle Data Group), p. 090001.

[10] Particle Data Group et al. "Review of Particle Physics". In: *Progress of Theoretical and Experimental Physics* 2022.8 (Aug. 2022), p. 083C01. ISSN: 2050-3911. DOI: 10.1093/ptep/ptac097. eprint: https://academic.oup.com/ptep/article-pdf/2022/8/083C01/49175539/ptac097.pdf. URL: https://doi.org/10.1093/ptep/ptac097.

[11] *OPAL Events at LEP1*. url: https://opal.web.cern.ch/Opal/events/opalpics.html. accessed on 21/05/2024.

[12] W. J. Stirling R. K. Ellis and B. R. Webber. *QCD and Collider Physics*. Cambridge University Press, 2003.

[13] Matteo Cacciari, Gavin P Salam, and Gregory Soyez. "The anti-ktjet clustering algorithm". In: *Journal of High Energy Physics* 2008.04 (Apr. 2008), pp. 063–063. ISSN: 1029-8479. DOI: 10.1088/1126-6708/2008/04/063. URL: http://dx.doi.org/10.1088/1126-6708/2008/04/063.

[14] Stefan Weinzierl. *Introduction to Monte Carlo methods*. 2000. arXiv: hep-ph/0006269 [hep-ph]. URL: https://arxiv.org/abs/hep-ph/0006269.

[15] Anosh Joseph. *Markov Chain Monte Carlo Methods in Quantum Field Theories: A Modern Primer*. Springer International Publishing, 2020. ISBN: 9783030460440. DOI: 10.1007/978-3-030-46044-0. URL: http://dx.doi.org/10.1007/978-3-030-46044-0.

[16] G. Peter Lepage. "A new algorithm for adaptive multidimensional integration". In: *Journal of Computational Physics* 27.2 (1978), pp. 192–203. ISSN: 0021-9991. DOI: https://doi.org/10.1016/0021-9991(78)90004-9. URL: https://www.sciencedirect.com/science/article/pii/0021999178900049.

[17] G. Peter Lepage. "Adaptive multidimensional integration: vegas enhanced". In: *Journal of Computational Physics* 439 (Aug. 2021), p. 110386. ISSN: 0021-9991. DOI: 10.1016/j.jcp.2021.110386. URL: http://dx.doi.org/10.1016/j.jcp.2021.110386.

[18] David Tong. *Lectures on Quantum Field Theory*. Chapter 5, Quantizing the Dirac Field, p.120. University of Cambridge. URL: https://www.damtp.cam.ac.uk/user/dt281/qft/qft.pdf.

[19] Vladyslav Shtabovenko, Rolf Mertig, and Frederik Orellana. "New Developments in FeynCalc 9.0". In: *Computer Physics Communications* 207 (2016), pp. 432–444.

[20] Wolfram Research Inc. *Mathematica, Version 13.1*. Champaign, IL, 2022.

[21] Pauli Virtanen et al. "SciPy 1.0: Fundamental Algorithms for Scientific Computing in Python". In: *Nature Methods* 17 (2020), pp. 261–272. DOI: 10.1038/s41592-019-0686-2.

[22] G. Peter Lepage. *Vegas: Adaptive Multi-dimensional Integration in Python*. DOI: 10.5281/zenodo.592154. URL: https://pypi.org/project/vegas/.

[23] A. Tumasyan et al. "Measurement of the top quark mass using a profile likelihood approach with the lepton+jets final states in protonproton collisions at $\sqrt{s} = 13\,\text{TeV}$". In: *The European Physical Journal C* 83.10 (Oct. 2023). ISSN: 1434-6052. DOI: 10.1140/epjc/s10052-023-12050-4. URL: http://dx.doi.org/10.1140/epjc/s10052-023-12050-4.

[24] J. Wissmann. "Heavy Quark Production at the LHC and its Impact on Parton Distribution Functions". Master's Thesis. University of Muenster, Sept. 2023.

[25] K. Kovarík et al. "nCTEQ15: Global analysis of nuclear parton distributions with uncertainties in the CTEQ framework". In: *Physical Review D* 93.8 (Apr. 2016). ISSN: 2470-0029. DOI: 10.1103/physrevd.93.085037. URL: http://dx.doi.org/10.1103/PhysRevD.93.085037.

[26] Aad et. al. "Measurement of the inclusive jet cross-section in proton-proton collisions at $\sqrt{s} = 7$ TeV using 4.5 fb1 of data with the ATLAS detector". In: *Journal of High Energy Physics* 2015.2 (Feb. 2015). ISSN: 1029-8479. DOI: 10.1007/jhep02(2015)153. URL: http://dx.doi.org/10.1007/JHEP02(2015)153.

[27] SHINE Collaboration et al. *Measurement of negatively charged pion spectra in inelastic p+p interactions at p_{lab} = 20, 31, 40, 80 and 158 GeV/c*. 2014. DOI: https://doi.org/10.1140/epjc/s10052-014-2794-6. arXiv: 1310.2417 [hep-ex]. URL: https://arxiv.org/abs/1310.2417.

Declaration of Academic Integrity

I hereby confirm that this thesis, entitled _____

_____ is solely my own work and that I have used no sources or aids other than the ones stated. All passages in my thesis for which other sources, including electronic media, have been used, be it direct quotes or content references, have been acknowledged as such and the sources cited. I am aware that plagiarism is considered an act of deception which can result in sanction in accordance with the examination regulations.

_____
(date, signature of student)

I consent to having my thesis cross-checked with other texts to identify possible similarities and to having it stored in a database for this purpose.

I confirm that I have not submitted the following thesis in part or whole as an examination paper before.

_____
(date, signature of student)